A PSEUDOSPECTRAL IMPLEMENTATION OF HAMILTONIAN SURFACE WATER WAVE EQUATIONS FOR COASTAL WAVE SIMULATION

by

ANDREW JOHNATHAN SCHAUF

B.S., Wichita State University, 2008

A thesis submitted to the

Faculty of the Graduate School of the

University of Colorado in partial fulfillment

of the requirement for the degree of

Master of Science

Department of Applied Mathematics

2013

This thesis entitled:

A pseudospectral implementation of Hamiltonian surface wave equations

for coastal wave simulation

written by Andrew Johnathan Schauf

has been approved for the Department of Applied Mathematics

Bengt Fornberg

Harvey Segur

Date _____

The final copy of this thesis has been examined by the signatories, and we

Find that both the content and the form meet acceptable presentation standards

Of scholarly work in the above mentioned discipline.

Schauf, Andrew J. (M.S., Applied Mathematics)

A pseudospectral implementation of Hamiltonian surface water wave equations for coastal wave simulation

Thesis directed by Professor Bengt Fornberg

A Hamiltonian formulation of surface water wave dynamics offers several useful features for numerical simulations of coastal waves, including reduction of the fully three-dimensional fluid problem to free surface variables and conservation of an approximated total energy. The spectral linear version of the Hamiltonian dynamical equations captures wavelength dispersion using a pseudodifferential operator, while higher-order approximations of the total energy lead to dynamical equations that incorporate nonlinear effects in terms of this operator. These models, derived for constant depth, are extended for use with varying-depth bathymetries by replacing the pseudodifferential operator with a symmetrized combination of several such operators evaluated at selected depths from the bathymetry at hand. This new operator is constructed so as to minimize its error from the true local-depth operator over the entire bathymetry, with priority given to wavelengths for which the most accurate modeling is desired. The resulting equations are implemented using a Fourier pseudospectral method, with damping regions used to manage the inherent periodic boundary conditions, source terms used to generate waves within the computational domain, and additional damping terms used to roughly simulate reflective interfaces. The implementation is validated by comparison to data from several benchmark experiments: a focusing wave group over uniform depth, irregular waves over a sloping bathymetry, and monochromatic waves over a challenging shoal bathymetry. The results demonstrate the promising ability of this approach to accurately simulate dispersive and bathymetric effects, and to achieve improved accuracy through the use of nonlinear terms. These improvements in accuracy, however, appear to be limited by the increasing degree of filtration of high-wavenumber modes required to control aliasing in models of increasing order. Finally, the implementation is demonstrated through simulations of realistic wave scenarios over actual coastal bathymetries.

"Lautan maha dalam
mukul dentur selama
nguji tenaga pematang kita"

– Chairil Anwar

for my Mom and Dad

Acknowledgements

My involvement in this project began with an inquiry to Prof. E. "Brenny" van Groesen and Dr. Andonowati about the research being conducted at their organization, LabMath-Indonesia. Our continued correspondence led to my year-long research assistantship at LMI, supported by a 2011-2012 Boren Fellowship from the US Department of Defense, during which the current research was undertaken. I am deeply grateful to Pak Brenny for taking me on as a student. As a mentor, he has given me an ideal balance of guidance and independence. Thanks also go to Bu Aan for her warm encouragement and for the inspiring environment she has created at Lawangwangi, home of LMI. For their professional and personal support, I thank my friends at LMI/Lawangwangi, including Didit Adytia, Dian Astuti, Ruddy Kurnia, Lie She Liam, Mira Melania, Meirita Ramdhani, Amanda Rudiawan, Andreas Parama Wijaya, and Mourice Woran. My colleagues at Institut Teknologi Bandung, especially Sri Redjeki Pudjaprasetya and her students, helped to broaden my perspective towards the research. For financial and logistical support of my project, I thank the National Security Education Program and the Institute of International Education. At the University of Colorado at Boulder, I would like to thank Bengt Fornberg, Natasha Flyer, and the Radial Basis Functions group. Harvey Segur provided some much-appreciated insight during the final stages of my thesis preparation. I am indebted to John Pellegrino for giving me invaluable research experience and perspective. Discussions with fellow students Yessa Hargono and Sarah Hart helped make my challenging times at CU much more navigable. Without the encouragement of Wichita State University professors Elizabeth Behrman, Tom DeLillo, Jason Ferguson, James C. Ho, and Thalia Jeffres, I may never have found my way into this line of work. Finally, for everything, my deepest gratitude and love goes to my family, Kendra Midkiff, Kerry VanBurkleo, and my parents Ron and Kathy Schauf.

Contents

List of Tables

List of Figures

CHAPTER I

INTRODUCTION

Motivation

For many applications that benefit from an understanding of water waves, numerical simulations can provide a powerful tool. Simulations of typical ocean waves occuring in a certain area can provide valuable information to help guide routine maritime shipping and fishing activities or coastal and offshore engineering projects. Simulations of extreme wave scenarios such as tsunamis can help scientists anticipate the potential effects to be expected should a similar event occur; risks can be assessed and especially vulnerable areas can be identified in advance so that the negative impacts of such disasters may be minimized.

While this sort of general, prior understanding of local wave behaviors is useful, increasingly sophisticated applications demand fast, accurate wave forecasts based on data supplied in real time. In many sensitive maritime operations such as the installation of offshore wind turbines, technicians must attempt to time certain maneuvers to coincide with relatively calm wave conditions. Numerical predictions of wave conditions in the immediate future, based on real-time buoy or radar measurements of surface waves, could greatly aid in these efforts. Similarly, if forecasters are to provide reliable, localized extreme wave warnings based on remotely-sensed wave height data, they need robust computational techniques that can adequately simulate the wave behaviors of interest in faster-than-physical time.

Numerical schemes that approach the problem in its most general forms—solving the full Euler or Navier-Stokes equations throughout the entire three-dimensional fluid

interior—can require computation times running many orders of magnitude greater than physical simulation times, rendering them impractical for these kinds of applications. On the other hand, many of the commonly-used simplifications of these models are inadequately robust for realistic coastal wave simulations, failing to correctly capture one or more important phenomena such as dispersion, nonlinearity, or bathymetric effects. Many applications, such as those described above, benefit from the development of approaches falling between these two extremes.

Objective

This thesis investigates the potential of Hamiltonian dynamical equations, implemented for coastal wave simulation using a pseudospectral method, to address the need for methods that provide a balance of computational efficiency and accurate modeling of important phenomena such as dispersion, nonlinearity, and bathymetric effects. Surface wave models that approximately encode internal fluid motions in terms of variables at the free surface (known as *Boussinesq* models) can provide alternatives to more computationally expensive, fully three-dimensional schemes. When expressed in terms of the appropriate variables at the free surface, the Euler equations for inviscid, irrotational, incompressible fluids exhibit a Hamiltonian structure. In addition to an elegant theoretical formalism, this Hamiltonian structure offers practical advantages: it can be used to accomplish a reduction of the problem's dimensionality—and thus of the magnitude of the computational task—in a way that guarantees that an approximated total energy is conserved. This conservative property is advantageous both in light of both physical and numerical considerations.

By adjusting the order of this energy approximation, the corresponding Hamiltonian dynamical equations can be derived to a chosen order, providing a useful versatility; the order of nonlinearity providing the most appropriate balance of accuracy and computational speed can be chosen to suit the simulation at hand. The linear Hamiltonian model derived for uniform-depth bathymetries captures wavelength dispersion using a pseudod-

ifferential operator. Higher-order expansions of the energy expression yield nonlinear terms that can be computed in terms of this operator. While direct, analytical incorporation of general bathymetric variations into this formulation is not straightforward, more numerically-based approaches can be used to model effects of varying-depth bathymetries while still retaining some of the useful simplicity of the uniform-depth model. Despite the decidedly "numerical" character of such an approach, its details can perhaps nonetheless be tuned so as to respect physics as well as possible in some sense. If so, a pseudospectral implementation of the Hamiltonian formulation of surface wave dynamics could represent an efficient, robust scheme for accurate simulations of dispersion, nonlinearity, and bathymetric effects in coastal waves.

In light of these promising characteristics, this thesis aims to validate a pseudospectral implementation of Hamiltonian surface wave equations. By simulating several benchmark cases, the implementation's ability to simulate the wave phenomena of interest is tested. Finally, this thesis aims to demonstrate the applicability of the approach through simulations of realistic coastal wave scenarios.

Arrangement of the Thesis

Chapter I introduces the motivations, objective, and arrangement of the thesis.

Chapter II discusses the Hamiltonian formulation of surface water wave dynamics and describes the derivation of linear and higher-order dynamical equations for waves over uniform-depth in terms of a pseudodifferential operator. The result is then extended to handle bathymetries of varying depth through the construction of a symmetrized variable-depth operator as a linear combination of multiple constant-depth operators, each evaluated at a representative depth from the bathymetry at hand.

Chapter III addresses the implementation of these dynamical equations using a pseudospectral method. Advantages and challenges of this method for coastal wave simulation are discussed. Details regarding the treatment of boundary conditions, damping regions, reflective interfaces, wave generation, and dealiasing within the implementation are dis-

cussed.

Chapter IV presents results from several benchmark simulations to validate a code that implements the ideas discussed in Chapters II and III. The ability of the implementation to conserve the approximate total energy is investigated briefly. Next, results of several benchmark case simulations are compared to experimental data. Simulations in one horizontal dimension (1HD) of a focusing wave group over a uniform-depth tank and irregular waves over a sloping bathymetry test the method's ability to accurately capture wavelength dispersion and bathymetric effects. Simulation of waves propagating over a shoal in two horizontal dimensions (2HD) tests its performance in simulating refraction and diffraction over the types of challenging bathymetries encountered in coastal waters.

In Chapter V, the approach is used to simulate realistic coastal wave scenarios using bathymetry data from actual coastal locations. First, a tsunami occurring off the coast of southwest Java, Indonesia is simulated as an initial value problem. The code is then used to simulate wind-type waves approaching the coast of Pelabuhan Ratu in West Java, Indonesia.

In Chapter VI, some final conclusions are offered.

CHAPTER II

DYNAMICAL EQUATIONS

Hamiltonian structure of surface water wave equations

The dynamics of inviscid fluid flow are described in their most general form by the Euler equations. In the case of an irrotational fluid—a typical assumption in the study of surface waves, and assumed to be a reasonable approximation for most of the applications to be addressed here—admits description of the fluids velocity field as the gradient of a potential

$$\mathbf{u} = \nabla_3 \Phi. \tag{II.1}$$

The further assumption of incompressibility, that is, zero divergence of the velocity field, implies that the velocity potential satisfies the Laplace equation

$$\operatorname{div} \mathbf{u} = \nabla_3 \cdot (\nabla_3 \Phi) = \nabla_3^2 \Phi. \tag{II.2}$$

So, for an inviscid, incompressible, irrotational fluid the Euler equations reduce to the Laplace equation in the interior,

$$\nabla_3^2 \Phi = 0 \text{ for } -h(\mathbf{x}) < z < \eta(\mathbf{x}), \tag{II.3}$$

along with two time-dependent conditions on the free surface:

$$\eta_t + \nabla \Phi \cdot \nabla \eta = \Phi_z \text{ at } z = \eta(\mathbf{x}, t), \tag{II.4}$$

$$\Phi_t + \frac{1}{2} |\nabla_3 \Phi|^2 + g\eta = 0 \text{ at } z = \eta(\mathbf{x}, t). \tag{II.5}$$

The kinematic boundary condition (II.4) is an expression of zero fluid flow across the free surface, and the dynamic boundary condition (II.5) describes the balance of normal

stresses across the free surface when surface tension is negligibly small. The impermeability of the bottom boundary is given by

$$\Phi_z + \nabla\Phi \cdot \nabla h(\mathbf{x}) = 0. \tag{II.6}$$

In the Hamiltonian formulation of mechanics, a quantity H, typically defined as the sum of potential energy P and kinetic energy K of a system, is expressed in terms of *canonical variables* known as *generalized coordinates* $\mathbf{q}$ and *generalized momenta* $\mathbf{p}$:

$$H(\mathbf{q}, \mathbf{p}) = P(\mathbf{q}, \mathbf{p}) + K(\mathbf{q}, \mathbf{p}). \tag{II.7}$$

A dynamical system is *Hamiltonian* if the dynamical equations for these canonical variables satisfy

$$\begin{cases} \frac{\mathrm{d}\mathbf{q}}{\mathrm{d}t} = \frac{\partial H}{\partial \mathbf{p}} \\ \frac{\mathrm{d}\mathbf{p}}{\mathrm{d}t} = -\frac{\partial H}{\partial \mathbf{q}} \end{cases}. \tag{II.8}$$

This structure guarantees that the Hamiltonian function H is conserved in time, since

$$\frac{\mathrm{d}H}{\mathrm{d}t} = \frac{\partial H}{\partial \mathbf{q}}\frac{\mathrm{d}\mathbf{q}}{\mathrm{d}t} + \frac{\partial H}{\partial \mathbf{p}}\frac{\mathrm{d}\mathbf{p}}{\mathrm{d}t} = -\frac{\mathrm{d}\mathbf{p}}{\mathrm{d}t}\frac{\mathrm{d}\mathbf{q}}{\mathrm{d}t} + \frac{\mathrm{d}\mathbf{q}}{\mathrm{d}t}\frac{\mathrm{d}\mathbf{p}}{\mathrm{d}t} = 0. \tag{II.9}$$

The expression of a physical system in terms of a Hamiltonian can provide deep insight into its underlying mathematical structure, while also guaranteeing useful stability properties and the applicability of certain numerical schemes in simulations of the system.

The Hamiltonian structure underlying the surface water wave problem (II.2)–(II.6) was initially investigated by Zakharov [15], Luke [12], Broer [5], and others. If free surface height $\eta(\mathbf{x}, t)$ and free surface velocity potential

$$\phi(\mathbf{x}, t) \equiv \Phi(\mathbf{x}, z = \eta(\mathbf{x}, t), t) \tag{II.10}$$

are identified as canonical variables, then for the Hamiltonian function H, defined as usual as the sum of potential and kinetic energies

$$H(\phi, \eta) = P(\phi, \eta) + K(\phi, \eta), \tag{II.11}$$

it can be shown that the dynamic boundary conditions(II.4) and (II.5) are equivalent to the Hamilton's equations

$$\begin{cases} \partial_t \eta = \delta_\phi H \\ \partial_t \phi = -\delta_\eta H \end{cases}, \tag{II.12}$$

generalized here from (II.8) for continuum canonical variables $\phi(\mathbf{x})$ and $\eta(\mathbf{x})$ through the use of variational derivatives. In this way, the underlying Hamiltonian structure of the surface water wave problem (II.2)–(II.6) is revealed. While, historically, this new perspective represented an important theoretical development in the mathematical study of water waves, it also suggests a practical means for deriving useful wave models: given an expression $H(\phi, \eta)$ approximating the total energy to some desired order of accuracy, Hamilton's equations (II.12) can be used to derive corresponding dynamical equations for ϕ and η that are guaranteed to conserve H in time.

Derivation of dynamical equations for constant depth

Computation of the Hamiltonian

In expressing the Hamiltonian in terms of the free surface variables, computation of potential energy term is straightforward (integrals in horizontal dimensions are assumed to extend from $-\infty$ to $+\infty$):

$$P = \int \mathrm{d}P = \int \left(\int_{-h(\mathbf{x})}^{\eta(\mathbf{x})} gz \mathrm{d}z \right) \mathrm{d}\mathbf{x} = \int \left(\frac{1}{2} g\eta(\mathbf{x})^2 - \frac{1}{2} gh(\mathbf{x})^2 \right) \mathrm{d}\mathbf{x}. \tag{II.13}$$

For cases with uniform depth h, the constant lower boundary term can be discarded without affecting derivatives of the Hamiltonian, and so we have potential energy term

$$P = \frac{1}{2} \int g\eta(\mathbf{x})^2 \mathrm{d}\mathbf{x} \tag{II.14}$$

expressed *exactly* in terms of η.

Obtaining a simple, explicit expression of kinetic energy

$$K = \int \mathrm{d}K = \frac{1}{2} \int \left(\int_{-h(\mathbf{x})}^{\eta(\mathbf{x})} |\mathbf{u}(\mathbf{x}, z)|^2 \mathrm{d}z \right) \mathrm{d}\mathbf{x} \tag{II.15}$$

in terms of η and ϕ, however, is not so straightforward, requiring some approximation. Using vector identities and the Laplace equation (II.2), the integrand can be expressed

as a divergence:

$$\begin{aligned} K &= \frac{1}{2}\int\left(\int |\mathbf{u}(\mathbf{x},z)|^2\,\mathrm{d}z\right)\mathrm{d}\mathbf{x} \\ &= \frac{1}{2}\int\left(\int [\nabla_3\Phi\cdot\nabla_3\Phi]\,\mathrm{d}z\right)\mathrm{d}\mathbf{x} \\ &= \frac{1}{2}\int\left(\int [\nabla_3\cdot(\Phi\nabla_3\Phi)-\nabla_3^2\Phi]\,\mathrm{d}z\right)\mathrm{d}\mathbf{x} \\ &= \frac{1}{2}\int\left(\int \nabla_3\cdot(\Phi\nabla_3\Phi)\,\mathrm{d}z\right)\mathrm{d}\mathbf{x}. \end{aligned} \tag{II.16}$$

By applying the divergence theorem, then, the kinetic energy throughout the fluid interior can be expressed as an integral over the free surface S:

$$\begin{aligned} K &= \frac{1}{2}\int\left(\int \nabla_3\cdot(\Phi\nabla_3\Phi)\,\mathrm{d}z\right)\mathrm{d}\mathbf{x} \\ &= \frac{1}{2}\int_S [(\Phi\nabla_3\Phi)\cdot\hat{\mathbf{n}}]_{z=\eta(\mathbf{x})}\mathrm{d}S \\ &= \frac{1}{2}\int \phi(\mathbf{x})[\nabla_3\Phi\cdot(\hat{\mathbf{z}}-\nabla\eta(\mathbf{x}))]_{z=\eta}\mathrm{d}\mathbf{x}. \end{aligned} \tag{II.17}$$

The task of expressing the Hamiltonian $H(\phi,\eta)$ now amounts to approximating the free surface normal velocity

$$[\nabla_3\Phi\cdot(\hat{\mathbf{z}}-\nabla\eta(\mathbf{x}))]_{z=\eta} \tag{II.18}$$

in terms of free surface variables η and ϕ. The order of this approximation will determine the order of accuracy of the resulting dynamical equations.

Linear Hamiltonian model

First, we discuss the derivation a linear model which leads naturally to a spectral formulation which, in the next section, will be expanded to higher-orders. The derivation that follows closely resembles that of Craig and Sulem [7]. Spectral formulations of related fluid dynamics problems have been explored in other work such as that of Ablowitz and Haut [1].

For a fluid with uniform bottom depth h, if deviations of the free surface η from its undisturbed elevation $z=0$ are considered to be negligibly small, the role of free surface velocity potential ϕ given in (II.10) is assumed by

$$\phi_0(\mathbf{x}) \equiv \Phi(\mathbf{x}, z=0) \tag{II.19}$$

and the bottom boundary condition (II.6) reduces to

$$\Phi_z(\mathbf{x}, z = -h) = 0. \tag{II.20}$$

The interior velocity potential Φ is thus that of a uniform-depth fluid layer.

Separation of variables on (II.2) with boundary conditions (II.19) and (II.20) yields a general solution of the form

$$\Phi(\mathbf{x}, z) = \sum_{\mathbf{k}} \phi_{0,\mathbf{k}} \frac{\cosh(k(z+h))}{\cosh(kh)} \tag{II.21}$$

where

$$k = |\mathbf{k}| = |k_x \hat{\mathbf{x}} + k_y \hat{\mathbf{y}}| \tag{II.22}$$

are the magnitudes of wavenumbers for plane waves modes propagating in the unbounded horizontal plane. Given this explicit expression for Φ, free surface normal velocity (II.18) is approximated as

$$\begin{aligned}
[\nabla_3 \Phi \cdot (\hat{\mathbf{z}} - \nabla\eta(\mathbf{x}))]_{z=\eta} &\approx [\Phi_z]_{z=0} \\
&= \sum_{\mathbf{k}} \frac{k \sinh(k(0+h))}{\cosh(kh)} \phi_{0,\mathbf{k}} e^{(\mathbf{k}\cdot\mathbf{x} - \omega t)} \\
&= \sum_{\mathbf{k}} k \tanh(kh) \phi_{0,\mathbf{k}} e^{(\mathbf{k}\cdot\mathbf{x} - \omega t)}.
\end{aligned} \tag{II.23}$$

where $\phi_{0,\mathbf{k}}$ are the amplitudes of plane waves components of $\phi_0(\mathbf{x})$ with wavenumber $\mathbf{k}$. Using the equivalence of $\mathbf{x}$- and $\mathbf{k}$-space inner products, the corresponding kinetic energy approximation is

$$\begin{aligned}
K_2(\phi) &= \frac{1}{2} \int \phi(\mathbf{x}) \left[\sum_{\mathbf{k}} k \tanh(kh) \phi_{0,\mathbf{k}} e^{(\mathbf{k}\cdot\mathbf{x} - \omega t)} \right] \mathrm{d}\mathbf{x} \\
&= \sum_{\mathbf{k}} \left(\frac{1}{2} \int \hat{\phi}(\mathbf{k}) [k \tanh(kh) \hat{\phi}(\mathbf{k})] \mathrm{d}\mathbf{k} \right)
\end{aligned} \tag{II.24}$$

where $\hat{\phi}(k)$ is the spatial Fourier transform of $\phi(x)$ and the subscript on K_2 indicates the order of the integrand in η and ϕ. Introducing a pseudodifferential operator D, defined in terms of its symbol such that

$$\widehat{D\phi(\mathbf{x})} \equiv \hat{D}(k)\hat{\phi}(\mathbf{k}) = k \tanh(kh) \hat{\phi}(\mathbf{k}), \tag{II.25}$$

kinetic energy can be expressed in physical space as

$$K_2(\phi) = \frac{1}{2}\int \phi(\mathbf{x})\left(D\phi(\mathbf{x})\right)\mathrm{d}\mathbf{x}. \tag{II.26}$$

The resulting approximate Hamiltonian,

$$H_2(\phi,\eta) = P(\eta) + K_2(\phi) = \frac{1}{2}\int \left[g\eta^2 + \phi(D\phi)\right]\mathrm{d}\mathbf{x}, \tag{II.27}$$

can be used to determine the corresponding dynamical equations by computing variational derivatives $\delta_\phi H_2$ and $\delta_\eta H_2$ according to (II.12).

These variational derivatives are computed by finding the first-order changes in the Hamiltonian associated with small perturbations to the variable in question:

$$\begin{aligned}
\langle \delta_\phi H_2, u\rangle &= \lim_{\epsilon\to 0}\frac{H_2\left(\phi+\epsilon u,\eta\right) - H_2\left(\phi,\eta\right)}{\epsilon} \\
&= \lim_{\epsilon\to 0}\frac{1}{\epsilon}\left[\frac{1}{2}\int\left(\phi+\epsilon u\right)D\left(\phi+\epsilon u\right)\mathrm{d}\mathbf{x} - \frac{1}{2}\int\phi D\phi\mathrm{d}\mathbf{x}\right] \\
&= \frac{1}{2}\int\left(\phi Du + uD\phi\right)\mathrm{d}\mathbf{x} = \frac{1}{2}\left[\langle\phi, Du\rangle + \langle u, D\phi\rangle\right] \\
&= \frac{1}{2}\left[2\langle D\phi, u\rangle\right] = \langle D\phi, u\rangle,
\end{aligned} \tag{II.28}$$

so that

$$\delta_\phi H_2 = D\phi. \tag{II.29}$$

Similarly,

$$\begin{aligned}
\langle \delta_\eta H_2, u\rangle &= \lim_{\epsilon\to 0}\frac{H_2\left(\phi,\eta+\epsilon u\right) - H_2\left(\phi,\eta\right)}{\epsilon} \\
&= \lim_{\epsilon\to 0}\frac{1}{\epsilon}\left[\frac{1}{2}\int g\left(\eta+\epsilon u\right)^2\mathrm{d}\mathbf{x} - \frac{1}{2}\int g\eta^2\mathrm{d}\mathbf{x}\right] \\
&= \frac{1}{2}\int\left(2g\eta\right)u\mathrm{d}\mathbf{x} = \langle g\eta, u\rangle,
\end{aligned} \tag{II.30}$$

yielding

$$\delta_\eta H_2 = g\eta. \tag{II.31}$$

Thus, by Hamilton's equations, (II.12), the Hamilton's equations corresponding to the Hamiltonian approximation (II.27) are

$$\begin{cases} \partial_t\eta = D\phi \\ \partial_t\phi = -g\eta \end{cases}, \tag{II.32}$$

and are linear in η and ϕ.

As is apparent from the second-order differential equations equivalent to the system (II.32), for example

$$\left(\partial_t^2 + gD\right)\eta = 0, \tag{II.33}$$

the system is satisfied by plane wave modes

$$\eta(\mathbf{x}, t) = \eta_{0,\mathbf{k}} e^{i\left(\mathbf{k}\cdot\mathbf{x} - \sqrt{g\hat{D}(k,h)}t\right)}, \tag{II.34}$$

revealing the familiar dispersion relation for linear surface waves,

$$\Omega(k) = \sqrt{g\hat{D}(k,h)} = \sqrt{gk\tanh(kh)}. \tag{II.35}$$

Thus the operator D is related to the linear dispersion relation $\Omega(k)$ by

$$\hat{D}(k) = \frac{1}{g}\Omega^2(k). \tag{II.36}$$

Higher-order models

To derive higher-order dynamical equations consistent with the Hamiltonian structure, the Hamiltonian (II.11) is expanded to higher order using improved approximations of free surface normal velocity (II.18). Relaxing the assumption of negligibly small deviations of η from $z = 0$, free surface normal velocity is given by

$$\left[\nabla_3\Phi \cdot (\hat{\mathbf{z}} - \nabla\eta(\mathbf{x}))\right]_{\eta(\mathbf{x})} = \Phi_z\left(\mathbf{x}, \eta(\mathbf{x})\right) - \eta_x\Phi_x\left(\mathbf{x}, \eta(\mathbf{x})\right) - \eta_y\Phi_y\left(\mathbf{x}, \eta(\mathbf{x})\right). \tag{II.37}$$

Since

$$\begin{aligned}\phi_x(\mathbf{x}) &= \left[\Phi_x\frac{\mathrm{d}x}{\mathrm{d}x} + \Phi_y\frac{\mathrm{d}y}{\mathrm{d}x} + \Phi_z\frac{\mathrm{d}z}{\mathrm{d}x}\right]_{z=\eta(\mathbf{x})} \\ &= \Phi_x\left(\mathbf{x}, \eta(\mathbf{x})\right) + \eta_x\Phi_z\left(\mathbf{x}, \eta(\mathbf{x})\right),\end{aligned} \tag{II.38}$$

and thus

$$\Phi_x\left(\mathbf{x}, \eta(\mathbf{x})\right) = \phi_x(\mathbf{x}) - \eta_x\Phi\left(\mathbf{x}, \eta(\mathbf{x})\right) \tag{II.39}$$

and, similarly,

$$\Phi_y\left(\mathbf{x}, \eta(\mathbf{x})\right) = \phi_y(\mathbf{x}) - \eta_y\Phi\left(\mathbf{x}, \eta(\mathbf{x})\right), \tag{II.40}$$

free surface normal velocity is given by

$$\begin{aligned}\left[\nabla_3\Phi\cdot\left(\hat{\mathbf{z}}-\nabla\eta(\mathbf{x})\right)\right]_{z=\eta} &= \Phi_z-\eta_x\left(\phi_x-\eta_x\Phi_z\right)-\eta_y\left(\phi_y-\eta_y\Phi_z\right)\\ &= \left(1+\eta_x^2+\eta_y^2\right)\Phi_z\left(\mathbf{x},\eta(\mathbf{x})\right)-\eta_x\phi_x-\eta_x\phi_y \end{aligned} \tag{II.41}$$

with everything except the free surface vertical velocity $\Phi_z\left(\mathbf{x},\eta(\mathbf{x})\right)$ expressed in terms of η and ϕ.

To express $\Phi_z\left(\mathbf{x},\eta(\mathbf{x})\right)$ in terms of free surface variables, we expand about its values at $z=0$. The operator D defined in (II.25) is used, as previously in the linear model, to compute the vertical derivative $\Phi_z(\mathbf{x},0)$, while Laplace's equation (II.2) allows the higher-order vertical derivatives appearing in the expansion to be expressed in terms of horizontal derivatives of the velocity potential ϕ_0 (II.19):

$$\begin{aligned}\Phi_{zz}(\mathbf{x},0) &= -\left[\Phi_{xx}(\mathbf{x},0)+\Phi_{yy}(\mathbf{x},0)\right]\\ &= -\left[\partial_{xx}+\partial_{yy}\right]\phi_0(\mathbf{x})=-\nabla^2\phi_0(\mathbf{x}).\end{aligned} \tag{II.42}$$

So, expanding about $z=0$,

$$\begin{aligned}\Phi_z(\eta) &= \Phi_z(0)+\eta\left[\Phi_{zz}(0)\right]+\tfrac{1}{2!}\eta^2\left[\Phi_{zzz}(0)\right]+\tfrac{1}{3!}\eta^3\left[\Phi_{zzzz}(0)\right]+\ldots\\ &= D\phi_0-\eta\nabla^2\phi_0-\tfrac{1}{2}\eta^2\nabla^2D\phi_0+\tfrac{1}{6}\eta^3\left(\nabla^2\right)^2\phi_0+\ldots\\ &= \left[D-\eta\nabla^2-\tfrac{1}{2}\eta^2\nabla^2D+\tfrac{1}{6}\eta^2\left(\nabla^2\right)^2+\ldots\right]\phi_0.\end{aligned} \tag{II.43}$$

To relate the factor ϕ_0 to the true free surface variable ϕ, we similarly expand in η around $z=0$:

$$\begin{aligned}\phi=\Phi(\eta) &= \Phi(0)+\eta\left[\Phi_z(0)\right]+\tfrac{1}{2!}\eta^2\left[\Phi_{zz}(0)\right]+\tfrac{1}{3!}\eta^3\left[\Phi_{zzz}(0)\right]+\cdots\\ &= \phi_0+\eta D\phi_0-\tfrac{1}{2}\eta^2\nabla^2\phi_0-\tfrac{1}{3!}\eta^3\nabla^2D\phi_0+\cdots\\ &= \left(1+\eta D-\tfrac{1}{2}\eta^2\nabla^2-\tfrac{1}{6}\eta^3\nabla^2D+\cdots\right)\phi_0.\end{aligned} \tag{II.44}$$

Using the relation

$$(1+A)^{-1}=1-A+A^2-A^3+\ldots, \tag{II.45}$$

the expansion (II.44) can be inverted to express ϕ_0 in terms of η and ϕ:

$$\begin{aligned}\phi_0 &= \left(1 + \left[\eta D - \frac{1}{2}\eta^2\nabla^2 - \frac{1}{6}\eta^3\nabla^2 D + \ldots\right]\right)^{-1}\phi \\ &= \left(1 - \left[\eta D - \frac{1}{2}\eta^2\nabla^2 - \frac{1}{6}\eta^2\nabla^2 D + \ldots\right] + \left[\eta D - \frac{1}{2}\eta^2\nabla^2 + \ldots\right]^2 - [\eta D + \ldots]^3 + \ldots\right)\phi \\ &= \left(1 - \eta D + \frac{1}{2}\eta^2\nabla^2 + \eta D\eta D + \frac{1}{6}\eta^3\nabla^2 D - \frac{1}{2}\eta^2\nabla^2\eta D - \frac{1}{2}\eta D\eta^2\nabla^2 - \eta D\eta D\eta D + \ldots\right)\phi.\end{aligned} \tag{II.46}$$

Finally, inserting the expression (II.46) for ϕ_0 into the expansion (II.43), Φ_z can be expressed explicitly in terms of ϕ and η as

$$\Phi_z = W_0 + W_1 + W_2 + W_3 + \ldots \tag{II.47}$$

where, having grouped terms by the number of factors of η appearing within,

$$W_0 = D\phi, \tag{II.48}$$

$$W_1 = \left[-\eta\nabla^2 - D\eta D\right]\phi, \tag{II.49}$$

$$W_2 = \left[D\eta D\eta D + \eta\nabla^2\eta D + \frac{1}{2}D\eta^2\nabla^2 - \frac{1}{2}\eta^2\nabla^2 D\right]\phi, \tag{II.50}$$

and

$$\begin{aligned}W_3 = \Bigg[&\frac{1}{6}\eta^3\left(\nabla^2\right)^2 + \frac{1}{2}\eta^2\nabla^2 D\eta D - \frac{1}{2}\eta\nabla^2\eta^2\nabla^2 - \eta\nabla^2\eta D\eta D \\ &-\frac{1}{2}D\eta^2\nabla^2\eta D - \frac{1}{2}D\eta D\eta^2\nabla^2 + \frac{1}{6}D\eta^3\nabla^2 D - D\eta D\eta D\eta D\Bigg]\phi.\end{aligned} \tag{II.51}$$

Substituting the expansion for Φ_z (II.47) into the expression of normal velocity (II.41) and then into kinetic energy integral (II.17) gives kinetic energy

$$K = \frac{1}{2}\int \phi\left[\left(1 + \eta_x^2 + \eta_y^2\right)\left(W_0 + W_1 + W_2 + W_3 + ...\right) - \eta_x\phi_x \ - \eta_y\phi_y\right]\mathrm{d}\mathbf{x}. \tag{II.52}$$

Again grouping terms of common order in η and ϕ, we write

$$K = K_2 + K_3 + K_4 + K_5 + \cdot \tag{II.53}$$

where

$$K_2 = \frac{1}{2}\int \phi W_0 \mathrm{d}\mathbf{x}, \tag{II.54}$$

$$K_3 = \frac{1}{2}\int \phi \left[W_1 - \eta_x \phi_x - \eta_y \phi_y\right] \mathrm{d}\mathbf{x}, \tag{II.55}$$

$$K_4 = \frac{1}{2}\int \phi \left[W_2 + \left(\eta_x^2 + \eta_y^2\right) W_0\right] \mathrm{d}\mathbf{x}, \tag{II.56}$$

and

$$K_5 = \frac{1}{2}\int \phi \left[W_3 + \left(\eta_x^2 + \eta_y^2\right) W_1\right] \mathrm{d}\mathbf{x}. \tag{II.57}$$

Variational derivatives of the Hamiltonian

$$H = P + K = P + \left(K_2 + K_3 + K_4 + K_5 + \cdots\right), \tag{II.58}$$

computed according to (II.12) as were (II.28) and (II.30), then give the dynamical equations

$$\begin{cases} \partial_t \eta = D\phi + N_{\eta,2} + N_{\eta,3} + N_{\eta,4} + \ldots \\ \partial_t \phi = -g\eta - N_{\phi,2} - N_{\phi,3} - N_{\phi,4} - \ldots \end{cases} \tag{II.59}$$

with second-order nonlinear terms

$$N_{\eta,2} = \left[W_1 - \eta_x \phi_x - \eta_y \phi_y\right], \tag{II.60}$$

$$N_{\phi,2} = \left[\frac{1}{2}\left(\phi_x^2 + \phi_y^2 - (D\phi)^2\right)\right], \tag{II.61}$$

third-order nonlinear terms

$$N_{\eta,3} = \left[W_2 + \left(\eta_x^2 + \eta_y^2\right) W_0\right], \tag{II.62}$$

$$N_{\phi,3} = \left[-W_0 W_1\right], \tag{II.63}$$

and fourth-order nonlinear terms

$$N_{\eta,4} = \left[W_3 + \left(\eta_x^2 + \eta_y^2\right) W_1\right], \tag{II.64}$$

$$N_{\phi,4} = \left[-\frac{1}{2}\left(2W_0 W_2 + W_1 W_1 + \left(\eta_x^2 + \eta_y^2\right) W_1\right)\right]. \tag{II.65}$$

Truncation of the Hamiltonian (II.58) leads to truncation of the dynamical equations (II.59) at a corresponding order, with truncated dynamical equations conserving the corresponding truncated Hamiltonian.

Extension to varying-depth bathymetries

Construction of variable-depth combination operator

In previous sections, assumption of a uniform bottom depth h for the fluid layer led to spectral dynamical equations involving a pseudodifferential operator (II.25) modeling linear wavelength dispersion over a fixed depth, with higher-order terms then computed in terms of this operator. In order to handle more general bathymetries while still retaining this simple spectral formulation, a quasi-homogeneous assumption is invoked. That is, wave dynamics around at some position $\mathbf{x}$ are assumed to be well-modeled by the uniform-depth equations with local depth $h(\mathbf{x})$. This seems especially reasonable when variations in depth occur at large spatial scales relative to the waves of interest.

In the context of numerical schemes such as finite differences, which approximate differential operators using local data values in physical space, quasi-homogenization of the relevant operators might amount to simply substituting the local value of the spatially-varying parameter into the operator stencil at each position. However, given the inherently non-local, wavenumber-dependent nature of the operators used here, the computational task becomes potentially unwieldy; although we may be interested in the effects of an operator defined for parameter $h(\mathbf{x})$ only in the immediate neighborhood of $\mathbf{x}$ itself, computations involving the pseudodifferential operator inherently require computation over the entire domain in wavenumber space. For a computational grid of N nodes, calculation of the solution associated with each unique $h(\mathbf{x})$ demands as many as N times as many computations per time step than for the flat-bottom case, with resulting increases in computational time of several orders of magnitude for typical grid sizes.

Alternatively, the operator can be computed for a limited number $M < N$ of representative depths h_j and its action at intermediate depths approximated as a linear combination of these results. That is, for a pseudodifferential operator L, a new variable-depth combination operator is defined by

$$L_{\approx}(h)\phi \equiv \sum_{j=1}^{M} \rho_j(h) L(h_j)\phi. \tag{II.66}$$

The coefficients $\rho_j(h)$ here could simply be partition of unity functions that geometrically localize the influence of each uniform-depth operator. More restrictively, the h-dependence of coefficients $\rho_j(h)$ can be chosen such that some physically-meaningful constraint is respected for the combination operator (II.66).

Selection of representative-depth operator coefficients

In their work with unidirectional waves van Groesen and van der Kroon [13] adapted a constant-depth pseudodifferential operator L for use with varying bathymetries by constructing such a combination operator using two representative depths: the minumum depth h_{min} and maximum depth h_{max} of the bathymetry at hand:

$$\hat{L}(h,k) \equiv \rho_1(h)\hat{L}(h_{min},k) + \rho_2(h)\hat{L}(h_{max},k). \tag{II.67}$$

Coefficients for these two operators were computed by solving a system of two constraints for each depth: first, they required that the composite operator should exactly satisfy the dispersion relation at all depths for waves of some chosen single frequency ν,

$$\hat{L}(h,K(\nu,h)) \equiv \rho_1(h)\hat{L}(h_{min},K(\nu,h)) + \rho_2(h)\hat{L}(h_{max},K(\nu,h)), \tag{II.68}$$

where $K(\omega,h)$ is the inverse of the dispersion relation $\omega = \Omega(k,h)$, and second, that intermediate-depth coefficients should be a partition of unity,

$$\rho_1(h) + \rho_2(h) = 1. \tag{II.69}$$

This approach could perhaps be generalized to a basis of more than two representative-depth operators by enforcing additional constraints, for example those involving related quantities such as group velocity. However, the use of several simultaneous, exact restrictions at single values may lead to highly unphysical results for other frequencies.

And so, instead of strictly imposing multiple physical conditions at a single frequency, we generalize upon the approach of van Groesen and van der Kroon [13] by choosing coefficients to minimize an expression of overall error on the operator at each depth. For each depth h, we approximate the true pseudodifferential operator L by a combination of operators $\hat{L}_j(k) = \hat{L}(h_j,k)$ as in (II.66). The sum of squared errors on the symbol of this

composite operator, as evaluated at discrete wavenumbers k of interest and supplied with some function $w(h,k)$ assigning greater weight to wavenumbers of greater importance in the simulation at hand, is then given by

$$E(h) = \sum_{k=k_{min}}^{k_{max}} w(h,k) \left(\hat{L}_{\approx}(h,k) - \hat{L}(h,k) \right)^2 = \frac{1}{2} \boldsymbol{\rho}(\mathbf{h})^{\mathbf{T}} \mathbf{Q} \boldsymbol{\rho}(\mathbf{h}) + \mathbf{f}^{\mathbf{T}} \boldsymbol{\rho}(\mathbf{h}) + \sum_{k=k_{min}}^{k_{max}} w(h,k) [\hat{L}(h,k)]^2, \tag{II.70}$$

where

$$\boldsymbol{\rho}(h) = \begin{bmatrix} \rho_1(h) \\ \vdots \\ \rho_M(h) \end{bmatrix}, \tag{II.71}$$

$$\mathbf{Q}(h) = 2 \sum_{k=k_{min}}^{k_{max}} w(h,k) \begin{bmatrix} \hat{L}_1(k)^2 & \cdots & \hat{L}_1(k)\hat{L}_M(k) \\ \vdots & \ddots & \vdots \\ \hat{L}_M(k)\hat{L}_1(k) & \cdots & \hat{L}_M(k)^2 \end{bmatrix}, \tag{II.72}$$

and

$$\mathbf{f}(h) = -2 \sum_{k=k_{min}}^{k_{max}} w(h,k) \hat{L}(h,k) \begin{bmatrix} \hat{L}_1(k) \\ \vdots \\ \hat{L}_M(k) \end{bmatrix}. \tag{II.73}$$

For each depth h, then, this expression of error is minimized for the optimizer $\boldsymbol{\rho}^*(h)$ of the quadratic programming problem with objective function

$$J(h) = \frac{1}{2} \boldsymbol{\rho}^{\mathbf{T}} \mathbf{Q} \boldsymbol{\rho} + \mathbf{f}^{\mathbf{T}} \boldsymbol{\rho}, \tag{II.74}$$

expressing the error (II.70), but omitting terms not dependent on coefficients $\boldsymbol{\rho}$.

The most appropriate choice of weight function $w(h,k)$ will depend on the wavenumber magnitudes k for which more accurate modeling is desired in a given case. For signaling problems, where waves are generated according to some signal $s(t)$ at some point or line within the domain, a natural choice is to assign priority proportionally based on the presence of corresponding modes in the spectrum of the influxed wave signal:

$$w(h,k) \propto \check{s}(\omega = \Omega(k,h)), \tag{II.75}$$

where $\check{s}(\omega)$ indicates the temporal Fourier transform. This can be seen as a generalization of the strict requirement that the approximation holds exactly true at a single frequency

ν as in (II.68), here represented by the special case

$$w(h,k) = \delta(k - K(\nu, h)) \tag{II.76}$$

corresponding to a monochromatic signal $s(t)$ with frequency ν. In some cases, initial value problems may be approached somewhat similarly. For initial conditions where the free surface height $\eta(\mathbf{x}, t = 0)$ is nearly zero everywhere except in the neighborhood of some disturbance localized near some $\mathbf{x_0}$, the spatial Fourier transform can be converted roughly to a frequency spectrum via the dispersion relation evaluated at local depth $h(\mathbf{x_0})$. This spectrum can then used to define the weight function as was the frequency spectrum $\check{s}(\omega)$ in (II.75).

Symmetrization of the variable-depth operator

The eigenvalues of an operator L are pure imaginary if and only if it is skew-symmetric, satisfying

$$L^* = -L. \tag{II.77}$$

For first-order partial differential equations, this property is associated with unidirectional propagation of wave modes without growth or decay. Omnidirectional wave equations involve compositions of two such skew-symmetric unidirectional wave operators and are thus symmetric, satisfying

$$(L^*)^2 = L^2. \tag{II.78}$$

In this way, the symmetric property of the operator D (II.25) is associated with stable propagation of wave modes without growth or decay. If, in the process of constructing the variable-depth combination operator (II.66) from multiple symmetric operators, some asymmetric part has been introduced, this can be discarded—and the desired symmetry recovered—by extracting just its symmetric part

$$D_{\approx,sym} = \frac{1}{2}\left[D_{\approx} + D^*_{\approx}\right], \tag{II.79}$$

for use in computations. The adjoint operator $D^*_{\approx}$ used here is the operator for which

$$\langle D_{\approx}\phi, \psi\rangle = \langle \phi, D^*_{\approx}\psi\rangle. \tag{II.80}$$

Starting with the left-hand side of (II.80),

$$\begin{aligned}
\langle D_{\approx}\phi, \psi\rangle &= \int \left[D_{\approx}\phi(x)\right]\phi(x)\mathrm{d}x = \int \left[\int \widehat{D_{\approx}}\hat{\phi}(k)e^{ikx}\mathrm{d}k\right]\psi(k)\mathrm{d}x \\
&= \int \left[\int \left(\sum_{j=1}^{M}\rho_j(h(x))\widehat{D_j}\right)\hat{\phi}(k)e^{ikx}\mathrm{d}k\right]\psi(x)\mathrm{d}x \qquad \text{(II.81)} \\
&= \sum_{j=1}^{M}\int \left[\rho_j(h(x))\int \widehat{D_j}\hat{\phi}e^{ikx}\mathrm{d}k\right]\psi(x)\mathrm{d}x \\
&= \sum_{j=1}^{M}\int \left(\int \widehat{D_j}\phi(k)\mathrm{d}k\right)\rho_j(h(x))\psi(x)\mathrm{d}x \\
&= \sum_{j=1}^{M}\langle D_j\phi, \rho_j(h(x))\psi\rangle = \sum_{j=1}^{M}\langle \phi, D_j\rho_j(h(x))\psi\rangle \\
&= \langle \phi, \left[\sum_{j=1}^{M} D_j\rho_j(h(x))\right]\psi\rangle \qquad \text{(II.82)}
\end{aligned}$$

where in the penultimate line we have used the symmetry of the individual constant-depth operators D_j. From the right-hand side of (II.80), the adjoint operator is identified as the operator for which

$$D^*_{\approx}\phi = \left[\sum_{j=1}^{M} D_j\rho_j(h(x))\right]\phi = \left[\sum_{j=1}^{M} D_j\left(\rho_j(h(x))\phi(x)\right)\right]. \qquad \text{(II.83)}$$

The symmetric part (II.79) of the variable-depth combination operator is then given by

$$D_{\approx,sym} = \frac{1}{2}\sum_{j=1}^{M}\left[\rho_j(h(x))D_j + D_j\rho_j(h(x))\right]. \qquad \text{(II.84)}$$

This operator replaces the constant-depth operator D in the dynamical equations (II.59) for computations involving varying-depth bathymetries.

Alternatively, in the construction of a variable-depth operator by (II.66), one may choose to deal directly with the operator L, the symbol of which is given by

$$\hat{L}\hat{\phi} = \Omega(k,h)\hat{\phi}, \qquad \text{(II.85)}$$

and compute coefficients in the combination operator $L_{\approx}$ to minimize error on the dispersion relation itself. In this case, skew-symmetry could be recovered by computing the skew-symmetric part $L_{\approx,skew}$ and then the operator D computed as

$$D_{\approx,sym}\phi = \frac{1}{g}L_{\approx,skew}(L_{\approx,skew}\phi). \qquad \text{(II.86)}$$

Although dealing directly with the dispersion relation in this way may be in some ways preferable to dealing with D, any potential advantages of computing the operator by this method come at a computational cost, since composition of the operator with itself doubles the number of Discrete Fourier Transforms per time step compared with an operator that need only be applied once. Thus, in the simulations of Chapters IV and V, the operator (II.84) is used.

CHAPTER III

PSEUDOSPECTRAL IMPLEMENTATION

Advantages and challenges

Given the emergence of the non-polynomial pseudodifferential operator D in the derivations of the Order 1 Hamiltonian model, a Discrete Fourier Transform of data into wavenumber space is the natural way of making numerical computations involving D. Given the further usefulness of this operator in computing higher-order perturbations to the dynamical equations, time evolution of nonlinear terms in wavenumber space also seems natural. However, given the spatial pointwise multiplications of functions involved in these nonlinear terms, as well as in the implementation of additional features to be discussed in this chapter, a hybrid spatial-spectral or *pseudospectral* numerical method is required.

Viewed as the limit case of finite difference (FD) stencils extended to the entire computational domain, a pseudospectral method provides spectral accuracy not offered by finite difference schemes, often requiring a lower resolution to achieve the same accuracy as FD methods [9]. In the case of the operator D, related to the dispersion relation by (II.36), use of a Fourier pseudospectral methods implies accurate handling of the linear wavelength dispersion described by $\Omega(k, h)$; in numerical schemes such as finite differences, which approximates derivatives using weighted combinations of local data values in physical space, more elaborate approaches are required to construct stencils designed to respect dispersion relations. Conveniently, in a pseudospectral method, computation

of spatial derivatives such as those appearing in the nonlinear dynamical equations (II.59) becomes a simple algebraic operation in wavenumber space.

A pseudospectral approach also introduces several challenges for simulations. Implementation of certain types of boundary conditions, or any spatially localized features within the computational domain, may not be as straightforward as in other methods. In particular, for simulations of coastal waves, flexible computational grid geometries are often desirable; computational nodes can be positioned to accomodate curved coastline interfaces, and node densities locally refined in areas where higher resolution is required or coarsened to increase efficiency where lower resolution is adequate. Whereas alternatives such as finite elements, radial basis function (RBF), or RBF-based finite difference (RBF-FD) methods are equipped to take on irregular node arrangments, Fourier pseudospectral methods are basically restricted to uniformly-spaced rectilinear grids due to the nature of Discrete Fourier Transform algorithms. For many applications, however, the efficiency and accuracy offered by a pseudospectral method outweigh these challenges.

For this simulations of Chapters IV and V, the computational domain is discretized in space using a Fourier pseudospectral method, yielding an ordinary differential equation corresponding to each wavenumber component. Solutions can then be advanced in time in Fourier transform space using a method of lines with any suitable numerical ordinary differential equation solver; here, time evolution is performed by an adaptive time step $4^{\text{th}}/5^{\text{th}}$-order Runge-Kutta solver (MATLAB's "ode45").

Damping regions

The periodic basis functions of the Fourier spectral method lead to inherently periodic boundary conditions which are generally not desirable in realistic simulations. To prevent outgoing waves from propagating across periodic boundaries and reentering the domain, damping terms are added to the dynamical equations and localized by multiplication with a spatially-varying characteristic function. We consider the time evolution associated with

a linear damping term added to the free surface elevation dynamical equation,

$$\partial_t \eta = \ldots - \alpha \chi_D(x) \eta \tag{III.1}$$

where $\chi_D(x)$ is some characteristic function which equals 0 within the simulation domain, 1 in fully-damped regions at the boundaries of the computational domain, and smoothly varies between 0 and 1 over a transition region, the length scale of which is on the order of several times the impinging wavelengths so as to minimize unphysical reflections of outgoing waves back into the domain.

To choose an appropriately-scaled coefficient α for the damping term, one can consider the behavior of the differential equation

$$\partial_t \eta = -\alpha \eta, \tag{III.2}$$

the solutions of which decay in time as

$$\eta(t) = \eta_0 e^{-\alpha t}. \tag{III.3}$$

Over a duration t, wave components propagating over depth h with phase velocity $c(k,h) = \frac{\Omega(k,h)}{k}$ through regions for which $\chi_D(x) = 1$ are expected to decay to a fraction $\epsilon = \frac{\eta(t)}{\eta_0} = e^{-\alpha t}$ of their initial amplitudes while covering a distance $d = |c(k,h)|t$. For a fully-damped region spanning a length d in the direction of wave travel, then, a choice of

$$\alpha = -\frac{|c(k,h)|}{d} \log(\epsilon) \tag{III.4}$$

guarantees that waves amplitudes will decay to within some desired small fraction ϵ of their original amplitude before exiting the damped region. Choice of such a conservative wavelength-dependent value for α can reduce unwanted reflections from the damping transition region and help to speed computations. So, to prevent waves from propagating through the periodic domain boundaries inherent to the Fourier pseudospectral method, damping terms are added to each of the dynamical equations:

$$\begin{cases} \partial_t \eta = D\phi + \ldots + \left[\frac{|c(k,h)|}{d} \log \epsilon \right] \chi_D(x) \eta \\ \partial_t \phi = -g\eta + \ldots + \left[\frac{|c(k,h)|}{d} \log \epsilon \right] \chi_D(x) \phi \end{cases} . \tag{III.5}$$

Embedded reflective interfaces

For wave damping by the method of the previous section, a smooth characteristic function $\chi_D(x)$ introduces damping gradually over a spatial scale on the order of the impinging wavelengths to minimize reflection of waves back into the computational domain. For modeling of reflective interfaces within the domain, however, this effect may be desirable. In regions where velocity potential ϕ is damped to approach a constant value of zero, the corresponding values of velocity $\mathbf{u}$ approach zero. If the characteristic function $\chi(x)$ changes over a very small spatial scale, this transition to zero velocity will occur abruptly, producing reflected waves. Thus, to roughly simulate reflections from objects within the domain, such a term is added to the velocity potential dynamical equation:

$$\begin{cases} \partial_t \eta = D\phi + \dots \\ \partial_t \phi = -g\eta + \dots + \beta\chi_R(x)\phi \end{cases} \tag{III.6}$$

where $\chi_R(x)$ transitions sharply from 0 to 1 where reflections are desired and β is some scalar chosen here in an ad hoc way. Empirical investigations suggest that reflectivity of interfaces depends in a predictable way on the slope of the factor $\beta\chi_R(x)$, and that partially-reflective interfaces could be modeled by an appropriate choice of a characteristic function to yield the desired reflective effects. Investigating the physicality of the reflections produced is beyond the scope of this thesis, however; here, the above terms are added merely as a crude means of simulating reflections. Addition of forcing terms, such as those described in the following section, may prove to be a superior method of introducing reflected waves into the domain and modeling a truly physical, zero-normal-velocity reflective condition.

Wave generation

In some cases, the wave scenario to be simulated can be approached as an initial value problem. Perhaps more often, however, simulations of realistic waves requires consideration of a signaling problem, especially where wave fields are to be predicted

based on some locally-measured wave signal.

To generate a wave field within the computational domain in accord with a signal specifying free surface heights at a specific spatial location with respect to time, a forcing term $G(x,t)$ can be added to the linear dynamical equations following the work of Wei et al. [14], Kim et al. [10], and Liam [11]:

$$\begin{cases} \partial_t \eta = D\phi + G(x,t) \\ \partial_t \phi = -g\eta \end{cases} . \tag{III.7}$$

Decomposition of the second-order system equivalent to (III.7) into backward- and forward-propagating wave equation factors,

$$(\partial_t^2 + gD)\eta = (\partial_t - A)(\partial_t + A)\eta = \partial_t G, \tag{III.8}$$

where

$$\widehat{A\eta} = i\Omega(k,h)\hat{\eta}, \tag{III.9}$$

suggests that the first-order forced unidirectional equation

$$(\partial_t + A)\eta = S(x,t) \tag{III.10}$$

can alternatively be considered. Multiplication of this by the backward-propagating wave equation operator leads to

$$(\partial_t - A)(\partial_t + A) = (\partial_t - A)S \tag{III.11}$$

so that this forcing is related to the forcing term G in (III.7) by

$$\partial_t G = (\partial_t - A)S. \tag{III.12}$$

Fourier transforms in both space and time (indicated for a function $S(x,t)$ by the notation $\bar{S}(k,\omega)$) of the forced one dimensional equation (III.10) leads to

$$\left[(-i\omega) + (i\Omega(k,h))\right]\bar{\eta}(k,\omega) = \bar{S}(k,\omega) \tag{III.13}$$

which, solved for $\bar{\eta}$ and transformed back into the (x,t)-domain, yields

$$\eta(x,t) = \int\int \frac{\bar{S}(k,\omega)}{i(\Omega(k,h) - \omega)} e^{i(kx-\omega t)} \mathrm{d}k\mathrm{d}\omega. \tag{III.14}$$

Enforcing the condition that the free surface heights at a fixed location $x = 0$ are specified by some signal $s(t)$ gives the condition

$$s(t) = \int \int \frac{\bar{S}(k,\omega)}{i(\Omega(k,h) - \omega)} e^{-i\omega t} \mathrm{d}k \mathrm{d}\omega. \tag{III.15}$$

Evaluation of this integral allows the condition to be solved to explicitly express the forcing term S associated with given signal $s(t)$.

For the case of a 1HD delta-function-type source, the approach yields forcing term

$$\check{G}(x,\omega) = \delta(x)\check{s}(\omega)\frac{\mathrm{d}\Omega}{\mathrm{d}k}(K(\omega)) \tag{III.16}$$

where the notation $\check{s}(\omega)$ indicates the temporal Fourier transform of $s(t)$. Assuming a delta-function-type line source along the y-axis in 2HD, for influxing of monochromatic waves of amplitude a propagating under a small angle θ_0 from the $+x$-direction, the approach gives the forcing term

$$G(x,y,t) = \delta(x)ae^{i(k_y^0 y - \omega_0 t)}\frac{\mathrm{d}\Omega}{\mathrm{d}k}(K(\omega_0))\cos\theta_0 \tag{III.17}$$

Since this condition is derived for linear equations, in some nonlinear simulations the linear equations are retained near the influx source, with nonlinear terms introduced smoothly as waves propagate outward from the source through multiplication by a characteristic function $\chi_{NL}(\mathbf{x})$ equal to 0 around the source and transitioning to 1 away from the source.

Dealiasing

In numerical solutions of nonlinear partial differential equations by a Fourier pseudospectral method, higher-order wave modes are introduced through the multiplications of wave components, and the limited resolution of the spatial discretization leads these to be misidentified as, or *aliased* to, other wave modes within the discretization. Accumulation of these resulting aliasing errors can lead to inaccuracy and computational instability. Various strategies are commonly used to prevent this aliasing, including the addition of artificial hyperviscosity terms to the dynamical equations, which tend to

smooth out high-wavenumber oscillations, or low-pass filtering of solutions by setting to 0 all components of the Discrete Fourier Transform corresponding wavenumbers k with $|k| > k_{cut}$. In the nonlinear simulations of Chapters IV and V, dealiasing is performed by applying the latter method of filtration at each time step of the computation. Cutoff wavenumbers are chosen in accord with "Orszag's two-thirds rule" and its generalization to higher-order nonlinearities, by which k_{cut} is chosen as the maximum cutoff wavenumber for which no wave modes from the unfiltered range are aliased back into the unfiltered range under the order n nonlinearity [8]:

$$k_{cut} = \frac{2}{n+1}. \tag{III.18}$$

This expression for k_{cut} suggests that in simulations, a tradeoff can be expected: the higher accuracy expected from models of increasing order may be countered by the decreases in effective computational resolution imposed to control aliasing.

CHAPTER IV

VALIDATION

Investigations of Hamiltonian conservation

Initial value problem over uniform depth

The Hamiltonian dynamical equations discussed in Chapter II were implemented in a MATLAB code using the pseudospectral method and features discussed in Chapter III. As a first means of validation, the Hamiltonian-conserving property of the implementation is investigated through some simple initial value problem examples. These numerical experiments are conducted using the Order 1 and Order 2 Hamiltonian models in 1HD with a computational grid spacing of 0.10 m, initially with undamped periodic boundary conditions.

First, a Gaussian-shaped free surface disturbance (Figure IV.1) initially at rest evolves over a uniform depth of 0.10 m.

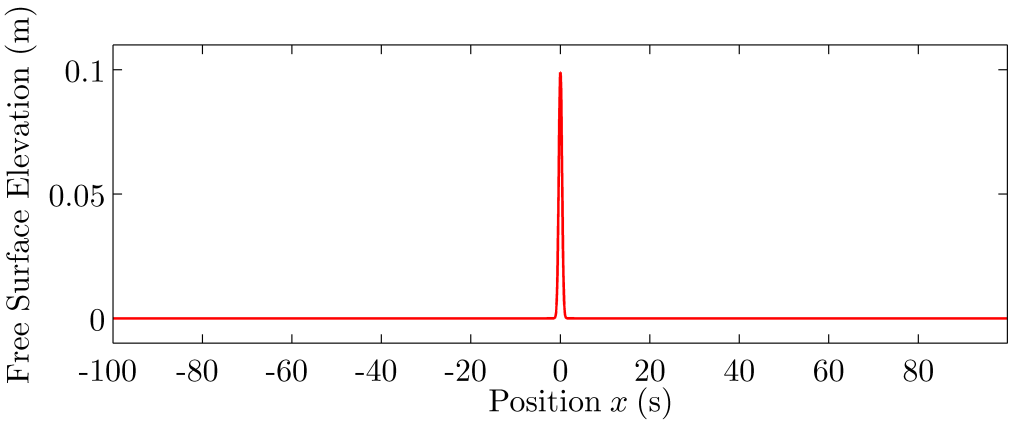

Figure IV.1: Initial free surface condition for investigations of Hamiltonian conservation

This combination of shallow depth and relatively large wave height highlights the differences of the Order 1 and Order 2 models: as Figure IV.2 shows, the initial condition propagates dispersively under the linear model, while under the Order 2 model, nonlinear effects counter this dispersive tendency as the initial condition separates into several apparently soliton-like features. The values of the Hamiltonian functions plotted

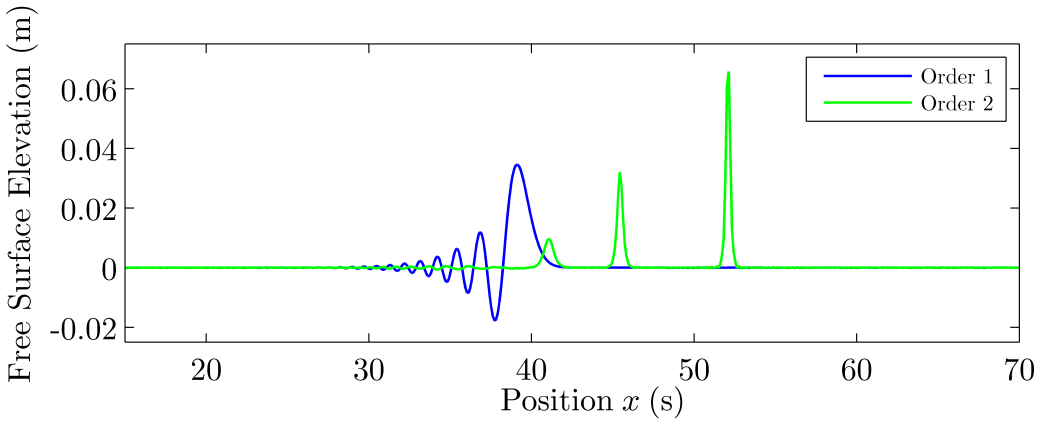

Figure IV.2: Comparison of Order 1 and Order 2 results over uniform depth at $t = 40$ s

in Figure IV.3, computed at each time step of the simulation by numerical approximation of the corresponding Hamiltonian integrals over the domain, confirm that both models manage to approximately conserve their respective Hamiltonians in time. Except for

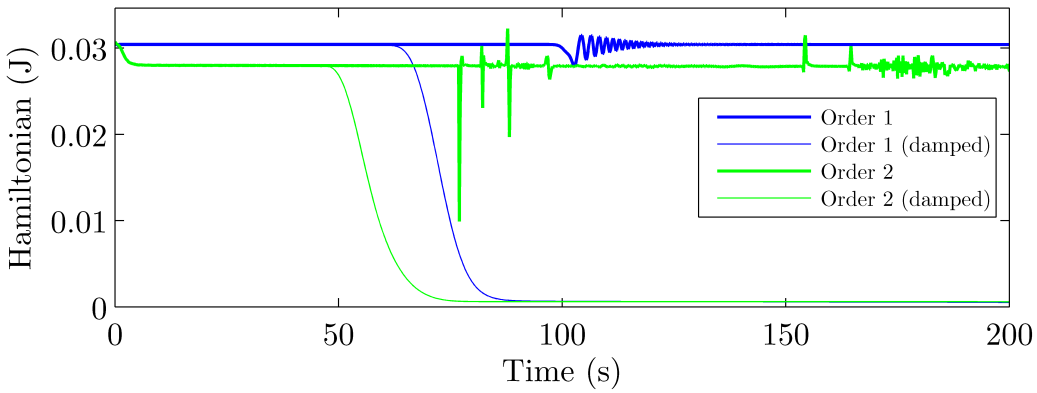

Figure IV.3: Evolution of Hamiltonian for the initial value problem over uniform depth

some fluctuations that occur when wave features collide and interfere, the values hold nearly constant. The Order 2 model drops slightly from its initial value as the initial

condition spreads outward, but quickly assumes an approximately constant value. Repeating the simulations with damping regions applied at the domain boundaries using the characteristic function shown in Figure IV.4 demonstrates that the Hamiltonian wave dynamics in the undamped domain are locally unaffected by the use of damping terms. Waves continue to evolve such that the Hamiltonian is conserved just as in the undamped

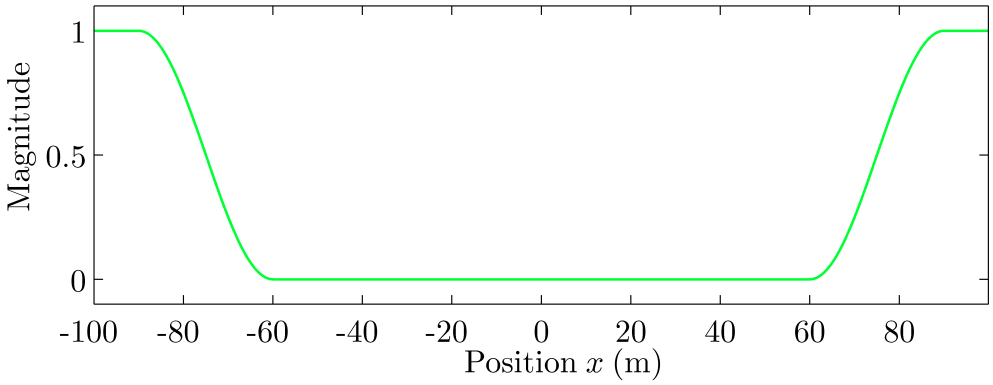

Figure IV.4: Damping region characteristic function $\chi_D(x)$ for simulation of initial value problem over uniform depth with damping

case (Figure IV.3) until entering the damping regions. The non-zero Hamiltonian value that persists after this damping is perhaps due to long wave components reflected from the damping region.

Initial value problem over varying-depth bathymetry

The Gaussian initial condition of Figure IV.1 now evolves from rest over the non-uniform bathymetry of Figure IV.5, beginning above a depth of 0.10 m as before, but then traveling over slopes into areas of depth 0.30 m. Again, undamped periodic boundaries are retained. Using a variable-depth operator constructed using 2 representative depths $h_1 = 0.10$ m and $h_2 = 0.30$ m to simulate the bathymetric variations, the Order 1 and Order 2 models again appear to approximately conserve their respective Hamiltonians (Figure IV.6). The Order 1 Hamiltonian indeed holds fairly constant around its initial value even as the waves transition into deeper waters. Just as before, the Order 2 Hamiltonian initially drops, but upon entering deeper water the waves assume a more

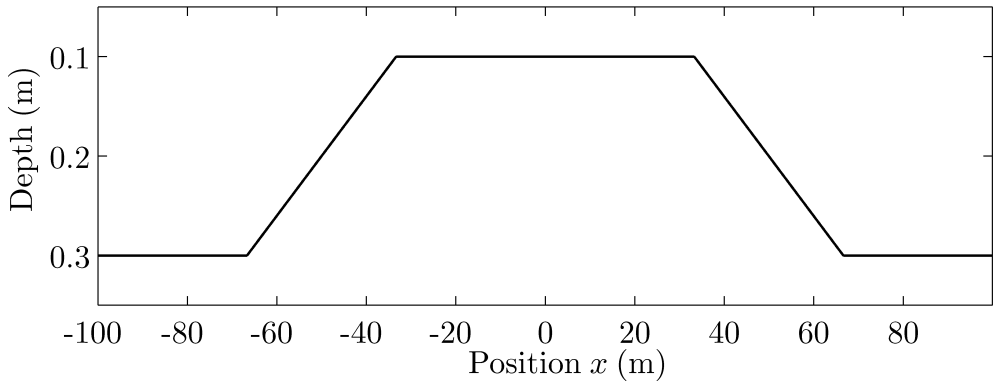

Figure IV.5: Bathymetry for initial value problem over varying depth

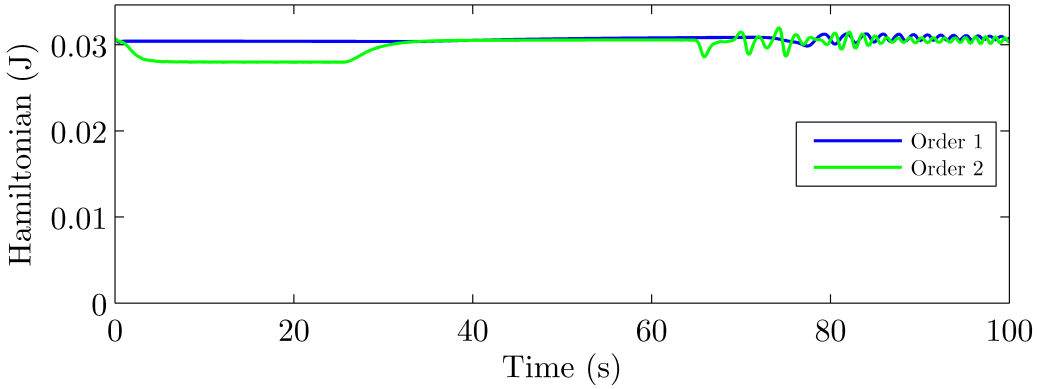

Figure IV.6: Evolution of Hamiltonian for the initial value problem over varying depth

dispersive behavior resembling that of the linear model (Figure IV.7), and the Hamiltonian increases towards its initial value again, where it remains as waves propagate over the deeper region.

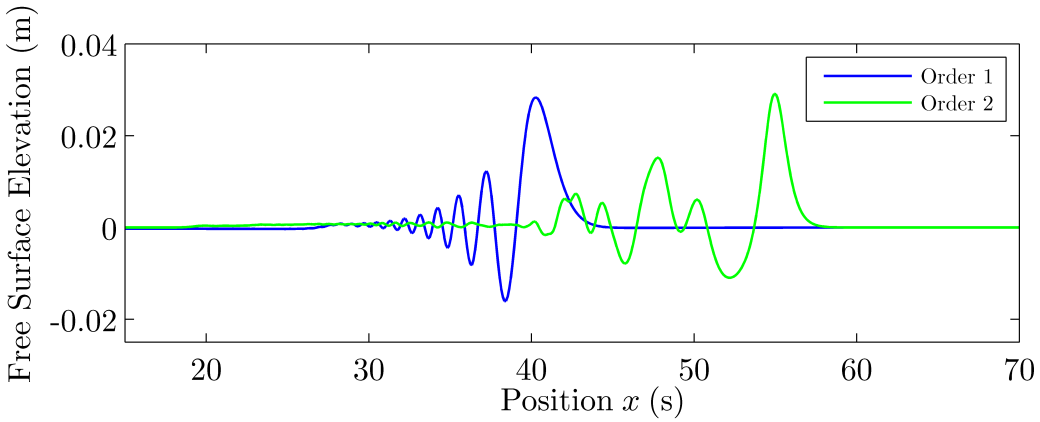

Figure IV.7: Comparison of Order 1 and Order 2 simulation results over varying depth at $t = 40$ s

Thus, the method of handling varying-depth bathymetries described in Chapter II appears capable of approximately retaining the desired Hamiltonian-conserving property of the uniform-depth models. Additional considerations may be useful to more deeply understand under which circumstances this holds true, as well as to understand the implications of the observed shifts in the nonlinear Hamiltonian's value as waves progressed above bathymetric variations.

Benchmark simulations in 1HD

1HD simulation of waves over constant depth

To investigate the capabilities of this approach to model and simulate wave phenomena of interest, the code is used to simulate scenarios for which experimental data is available for comparison. The first of these benchmarking experiments were conducted in the wave laboratories at Maritime Research Institute Netherlands (MARIN) [6]. These experiments involve wave basins with piston-type wave generators installed along one edge. Long-crested waves propagate along the length of the tank, with wave heights

measured by probes at several locations. At the other end of the basin, waves encounter a "beach" designed to minimize wave reflection. For these cases, this setup results in the propagation of long-crested waves, relatively uniform across the width of the tank, over bathymetries that are uniform across the width of the tank, and so the scenarios are simulated in 1HD.

The first case ("Wave groups propagating over a flat bottom: Run number 203001") involves a focusing wave group propagating over a uniform 1.00-m depth [6]. Waves are generated at $x = 0$ m and free surface elevations are recorded at 6 locations spanning the length of the basin as shown in Figure IV.8. For the simulation, the free surface elevations measured at position W1 are used as an influx signal for a delta-function-type source located there. To generate this focusing wave, initial oscillations of shorter

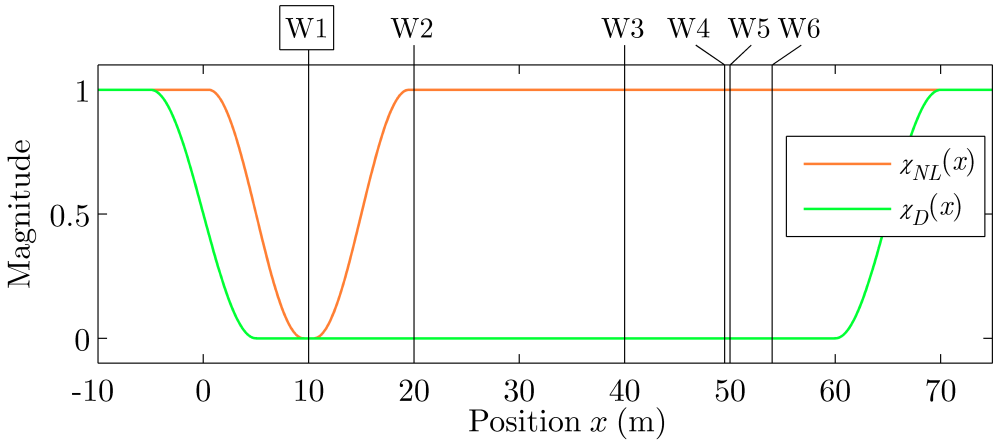

Figure IV.8: Measurement positions and characteristic functions for focusing wave simulation

wavelength transition gradually transition into longer waves so that the higher-speed, longer-wavelength wave features catch up with lower-speed, shorter-wavelength features to constructively interfere around W6. This progression is visible in the data measured at W1 (Figure IV.9), the spectrum of which is shown in Figure IV.10.

Damping regions are positioned beyond the outermost measurement locations W1 and W6 using a characteristic function $\chi_D(x)$ as shown in Figure IV.8. For nonlinear simulations, the characteristic function $\chi_{NL}(x)$ (Figure IV.8) introduces nonlinear terms gradually for waves propagating outward from the influx source at W1. Using the com-

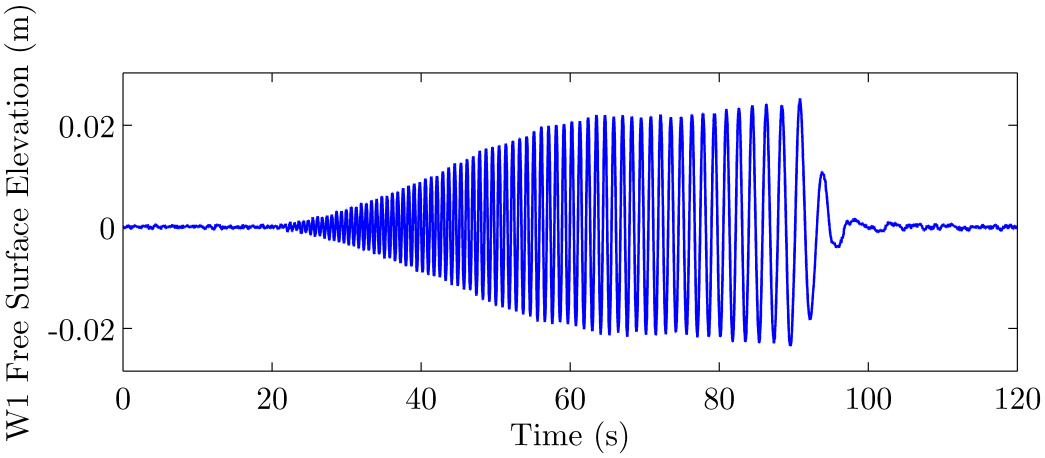

Figure IV.9: Measured signal at position W1 from focusing wave experiment

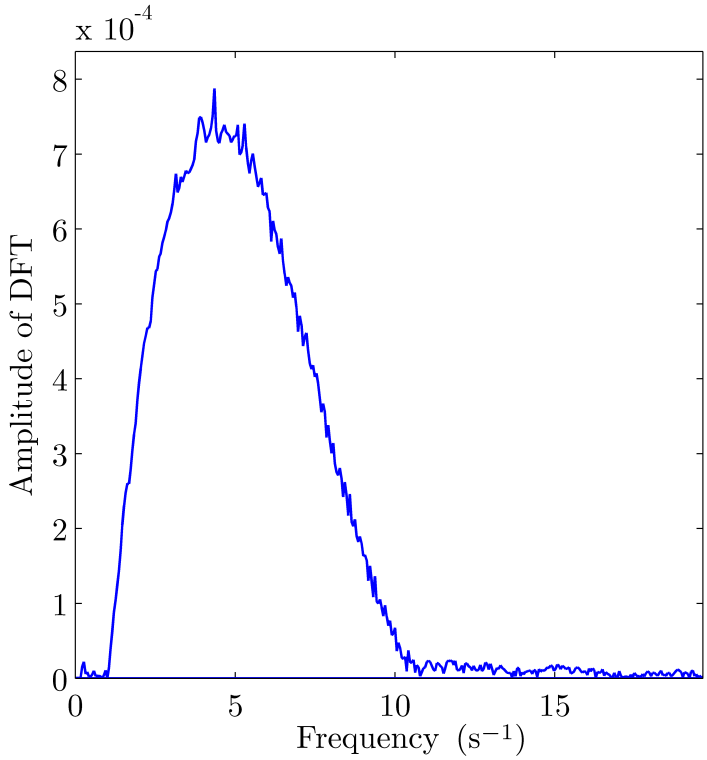

Figure IV.10: Frequency spectrum of measured signal at position W1 from focusing wave experiment

putational domain and characteristic functions shown in Figure IV.8 with a spacing of 0.10 m between computational nodes, the measured signal from position W1 is input as an influx signal to simulate the experiment.

Inspection of maximum and minimum wave height plots from the simulation reveals that the models correctly simulate dispersion to yield the constructive wave peak at the correct time and location. Comparison of the measured and simulated signals at W4 in

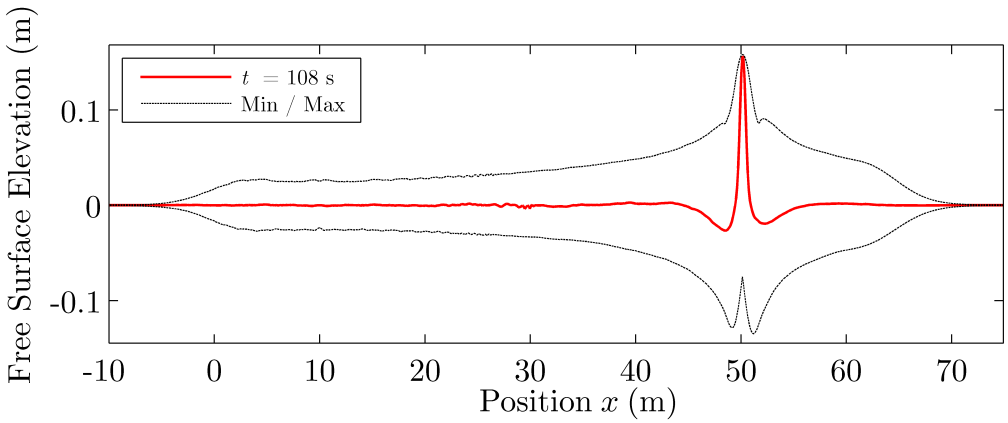

Figure IV.11: Free surface elevations at $t = 108$ s and max./min. wave heights for Order 1 focusing wave group simulation

Figure IV.12, as well as their spectra in Figure IV.13 demonstrates the superior prediction of wave heights and shapes by the nonlinear models.

As expected, the spectrum of the Order 1 model signal at W4 appears to be preserved from the influx at W1. The nonlinear models bring the W4 spectrum into better agreement with the measured spectrum. However, both the signals and spectra do not appear to improve much above Order 2, perhaps even becoming less accurate.

Signal correlations

$$C(\mathbf{x}) = \frac{\langle \eta(\mathbf{x},t)_{sim}, \eta(\mathbf{x},t)_{data} \rangle}{\langle \eta(\mathbf{x},t)_{data}, \eta(\mathbf{x},t)_{data} \rangle} \tag{IV.1}$$

for measured wave signals η_{data} with the simulated signals η_{sim} predicted by the Hamiltonian models are compared at each of the measurement locations in Table IV.1. These correlations reveal a significant improvement in accuracy from the Order 1 model to the Order 2 model, especially for larger distances from the influx source as the relatively high-amplitude focusing wave is produced. However, for higher-order models, correla-

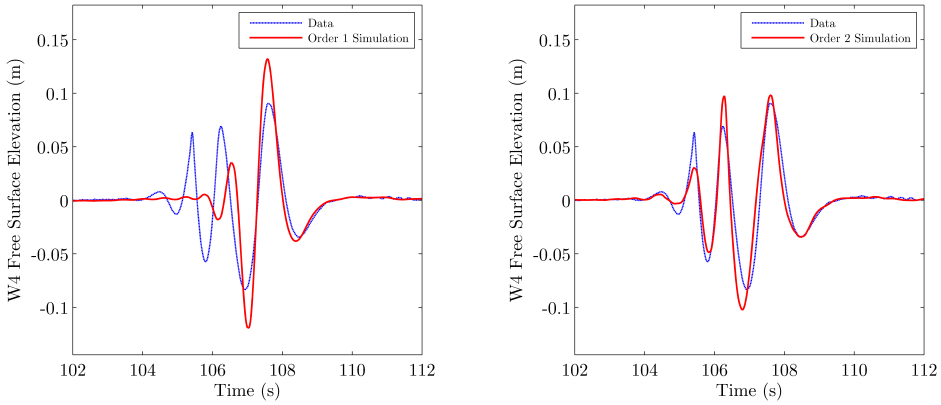

(a) Order 1 model

(b) Order 2 model

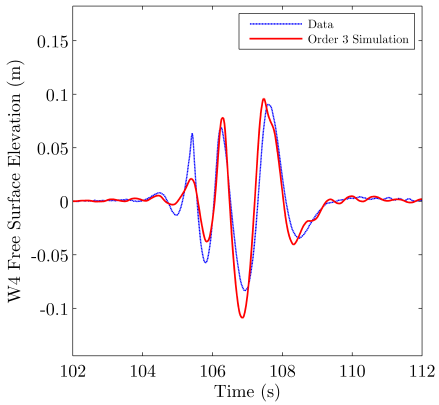

(c) Order 3 model

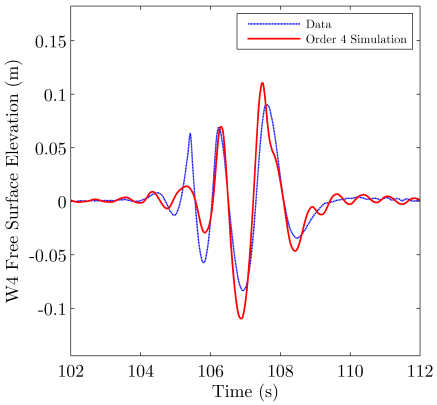

(d) Order 4 model

Figure IV.12: Comparison of measured and simulated signals at position W4 from focusing wave simulation

tions do not show significant improvement, with correlations actually tending to decline beyond Order 2. Although the correlation provides a somewhat limited glimpse into the relative performances of these models, this behavior seems to confirm the trend visible in Figures IV.12 and IV.13: it appears that, at least for this case and this choice of computational grid, the accuracy of higher-order models here is limited by the increasingly invasive dealiasing measures required. Perhaps in this truncation of higher-order wave modes, important wave information is indeed being discarded.

While the details of the simulation at hand will determine the usefulness of higher-

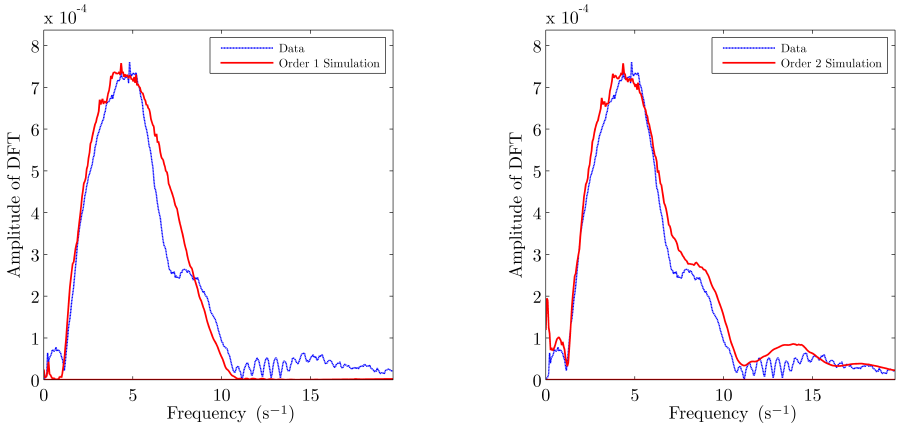

(a) Order 1 model

(b) Order 2 model

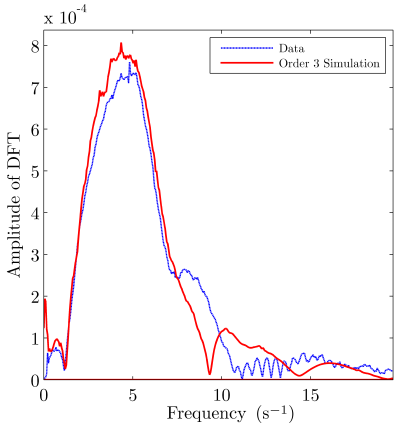

(c) Order 3 model

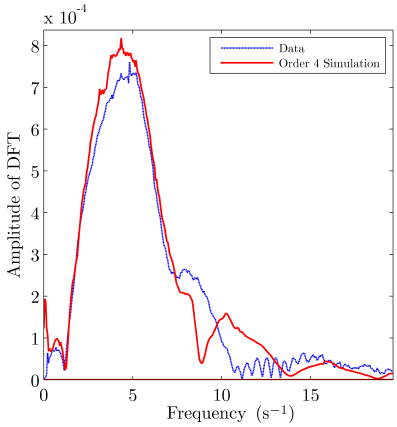

(d) Order 4 model

Figure IV.13: Comparison of measured and simulated spectra at position W4 from focusing wave simulation

order nonlinear models, the above results seem to indicate that models higher than Order 2 may not offer many advantages in some cases, especially considering the steep increases in computational time involved. In running this simulation, for example, the Order 2, 3, and 4 model codes required computational times of roughly 1.5, 2.5, and 5.5 times longer than the Order 1 model, respectively.

Finally, the evolution of the Hamiltonian function over the course of the simulation (Figure IV.14) appears to confirm the expected conservation of the Hamiltonian. During the period from around 103 s to 111 s, when no major waves are being influxed or damped,

Model	W2	W3	W4	W5	W6
Order 1	.971	.973	.753	.760	.700
Order 2	.973	.968	.920	.922	.863
Order 3	.973	.972	.919	.916	.832
Order 4	.974	.974	.900	.890	.838

Table IV.1: Correlations of simulation results with measurements for focusing wave group experiment

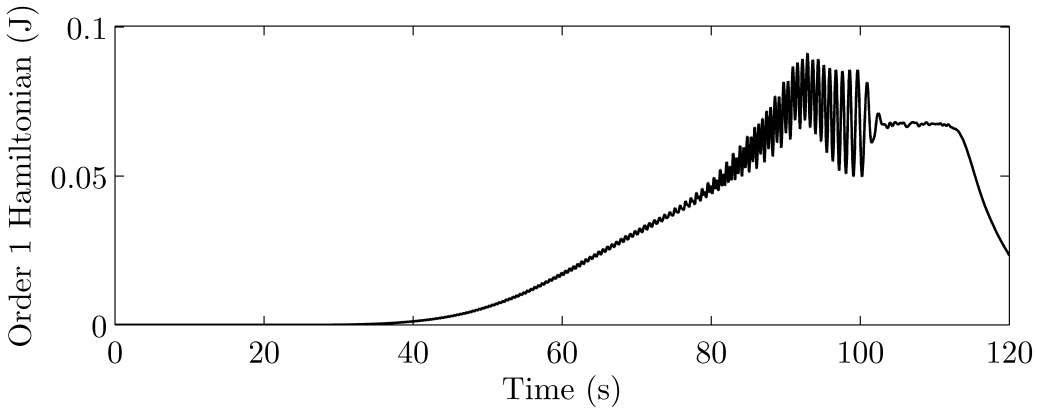

Figure IV.14: Evolution of Order 1 Hamiltonian for Order 1 simulation of focusing wave

the value holds approximately constant, even as the focusing wave peaks around 108 s. Higher-order expressions of the Hamiltonian, computed for higher-order simulations, show similar behavior.

1HD simulation of waves over sloping bottom

To validate the modeling of bathymetric effects by the code, a similar MARIN benchmark case is simulated, but this time over a varying-depth tank consisting of two uniform-depth areas with depths of 0.60 m and 0.30 m joined by a 1:20 sloping region as shown in Figure IV.15 ("Irregular waves propagating over a slope: Run number 102003") [6]. Waves generated at $x = 0$ m propagate along the length of the tank and free surface elevations are measured at 8 locations as also shown in Figure IV.15. For the simulation, measurements from location W1 are used as an influx signal for a delta-function-type source located there. This signal consists of irregular waves, the frequency spectrum of which is shown in Figure IV.16. As seen in Figure IV.17, damping regions are located

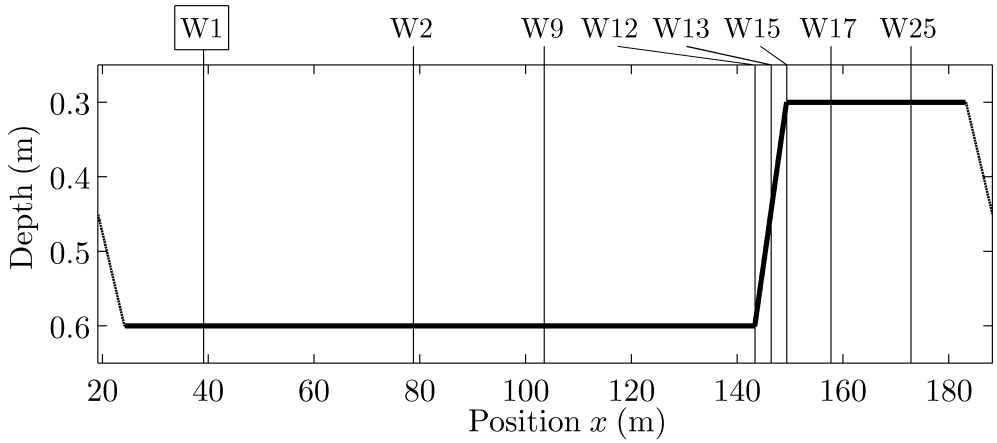

Figure IV.15: Bathymetry and measurement positions for sloping bathymetry experiment and simulation

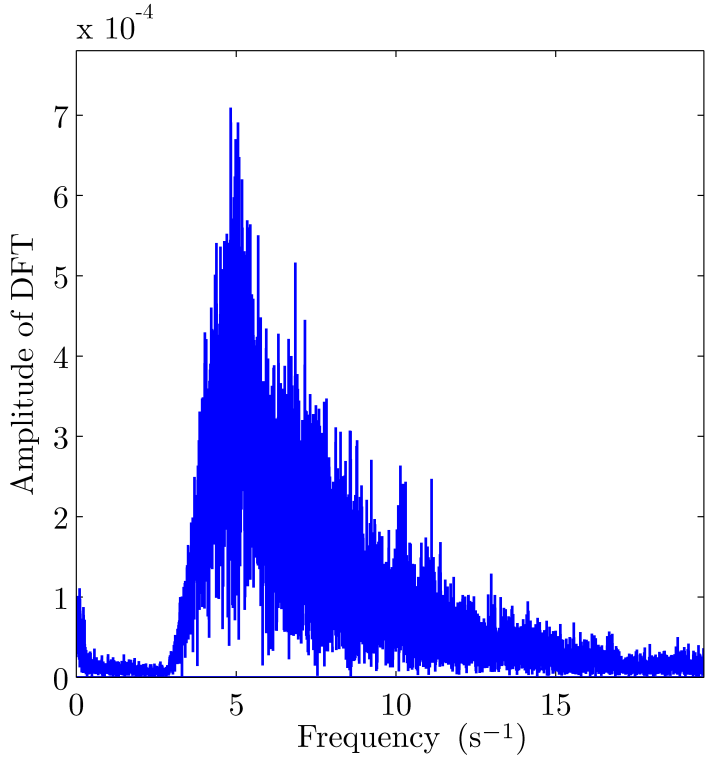

Figure IV.16: Frequency spectrum of measured signal at position W1 from sloping bathymetry experiment

beyond the outermost measurement points W1 and W25.

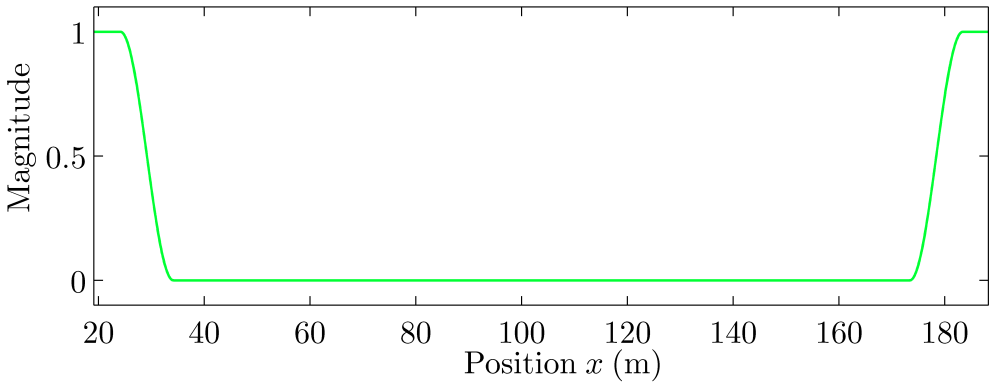

Figure IV.17: Damping region characteristic function $\chi_D(x)$ for sloping bathymetry simulation

For this bathymetry, a variable-depth operator is constructed as in (II.66) using three representative-depth operators with $h_1 = 0.3$ m, $h_2 = 0.42$ m, and $h_3 = 0.6$ m (Figure IV.18). Using weight function $w(h, k)$ (Figure IV.19) derived from the spectrum

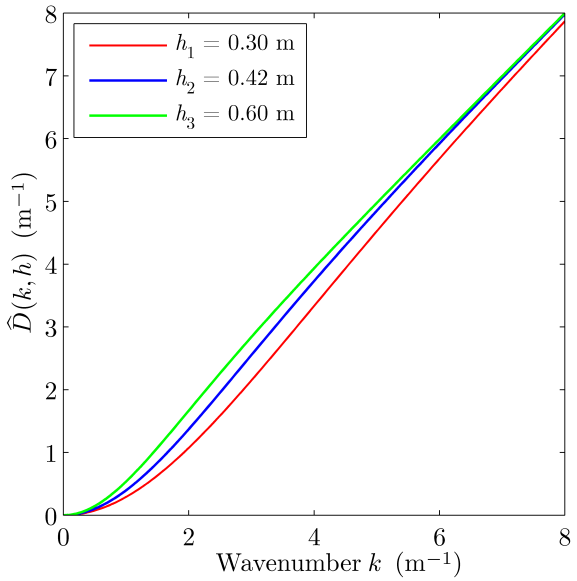

Figure IV.18: Representative-depth operators for sloping bathymetry simulation

of the W1 influx signal, the coefficients resulting from the optimization of (II.74) (Figure IV.20) produce a variable-depth operator with errors shown in Figure IV.21.

Inspection of signals at the measurement points demonstrate that the shifts in amplitude and wavelength for waves propagating over the slope are well-simulated (Fig-

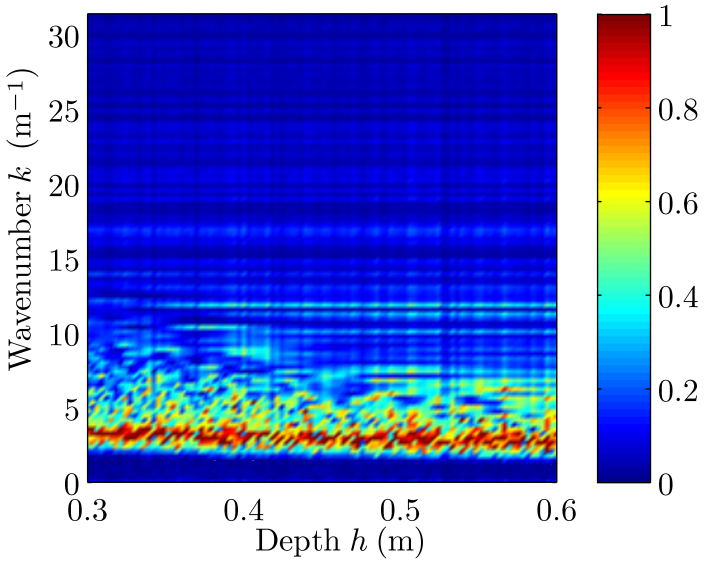

Figure IV.19: Weight function $w(h, k)$ for sloping bathymetry simulation

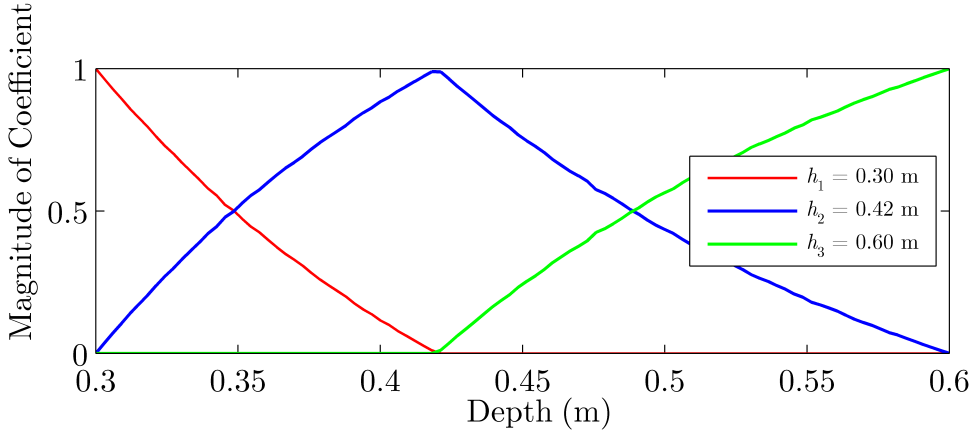

Figure IV.20: Representative-depth operator coefficients for sloping bathymetry simulation

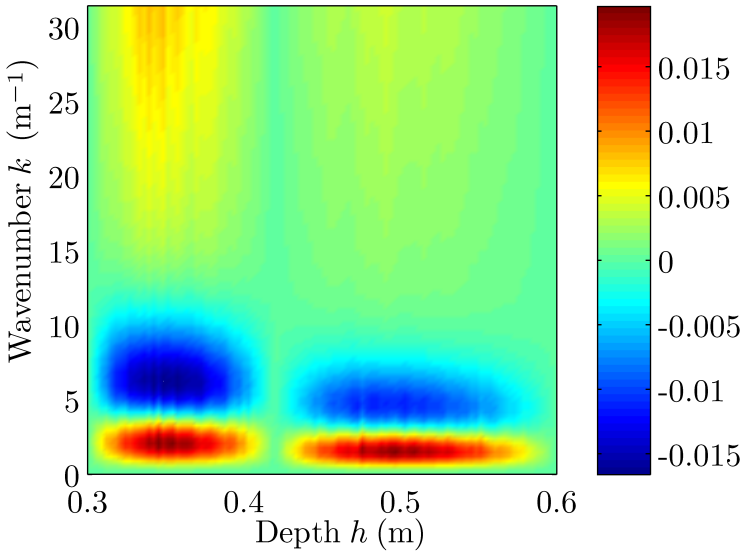

Figure IV.21: Error $\hat{D}_{\approx}(h,k) - \hat{D}(h,k)$ (m^{-1}) of variable-depth operator for sloping bathymetry simulation

Model	W2	W9	W12	W13	W15	W17	W25
Order 1	.702	.605	.662	.606	.614	.649	.489
Order 2	.787	.741	.381	.733	.725	.616	.554

Table IV.2: Correlations of simulation results with measurements for sloping bathymetry experiment

ures IV.22–IV.25). As is visible in the plots, the Order 2 model often more successfully predicts wave shapes, especially, it seems, for large-amplitude wave features. This trend again tends to be supported by signal correlation values (Table IV.2). The results demonstrate that the methods described in Chapter II can be an accurate means of simulating bathymetric effects in varying-depth waters such as those encountered in coastal wave simulations.

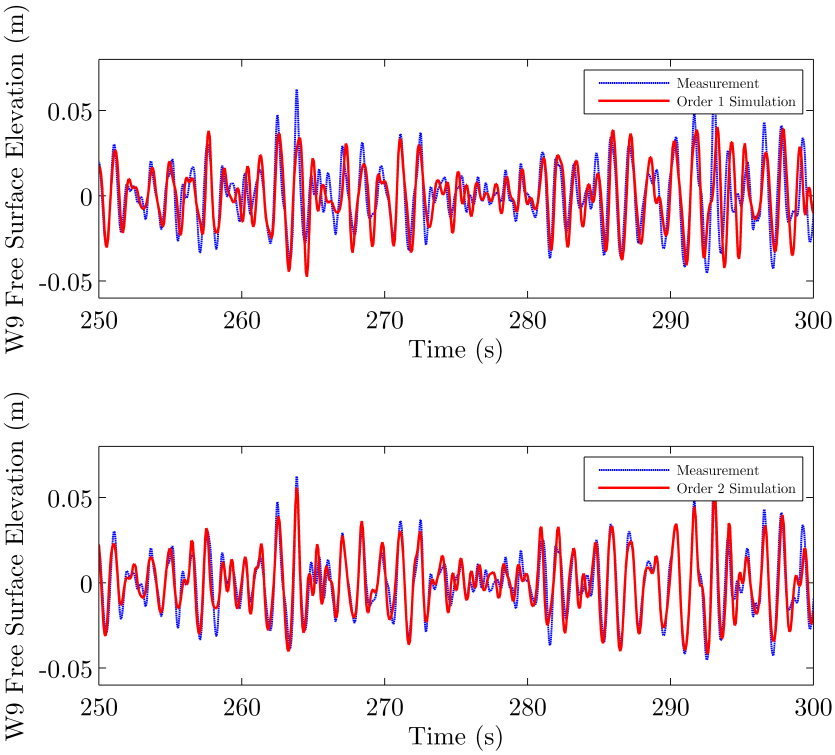

Figure IV.22: Comparison of measured and simulated wave signals at W9 from sloping bathymetry simulation

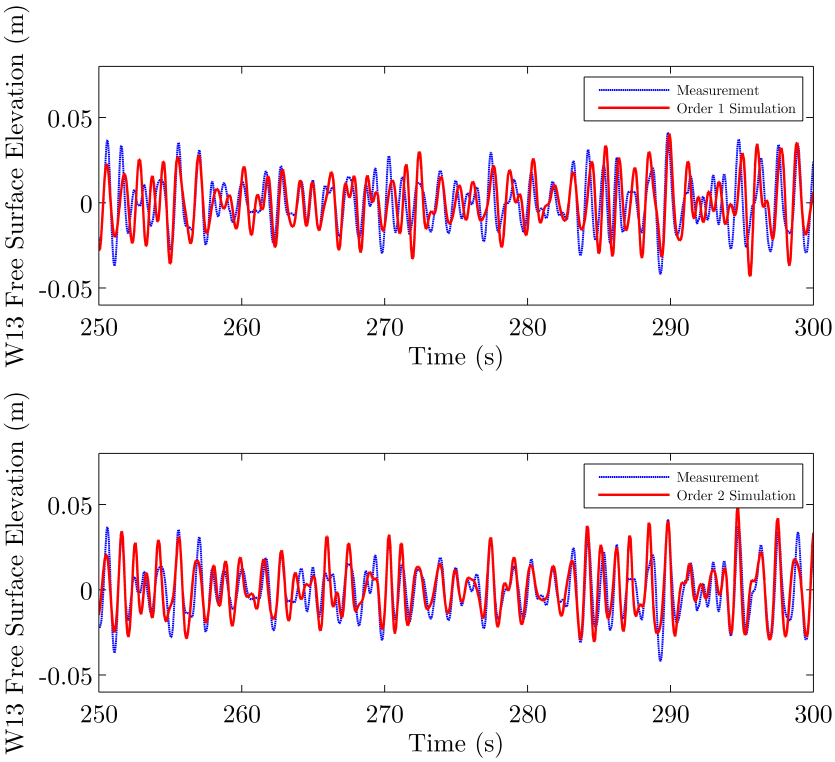

Figure IV.23: Comparison of measured and simulated wave signals at W13 from sloping bathymetry simulation

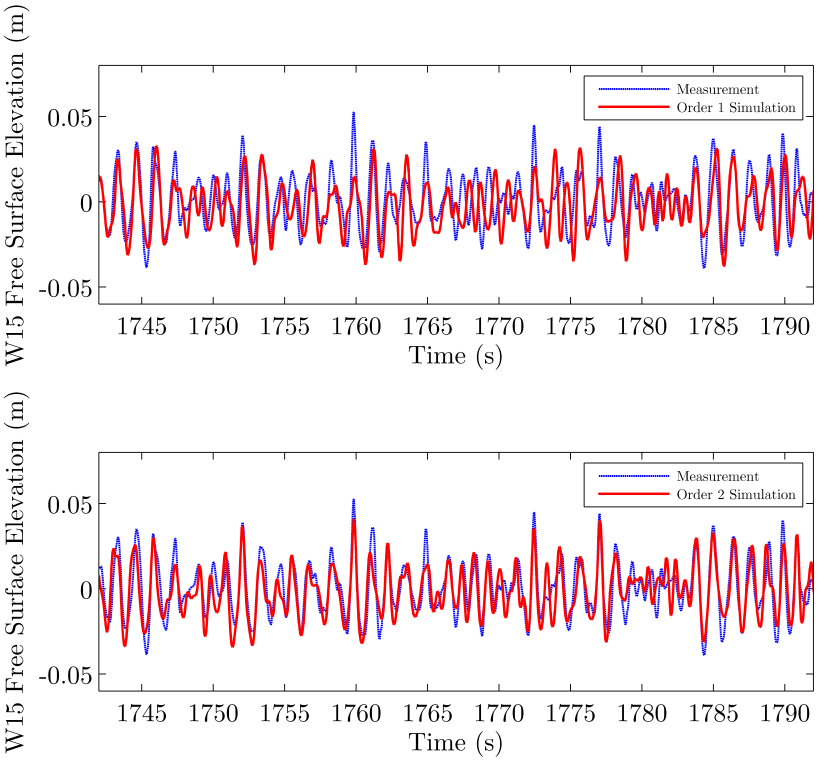

Figure IV.24: Comparison of measured and simulated wave signals at W15 from sloping bathymetry simulation

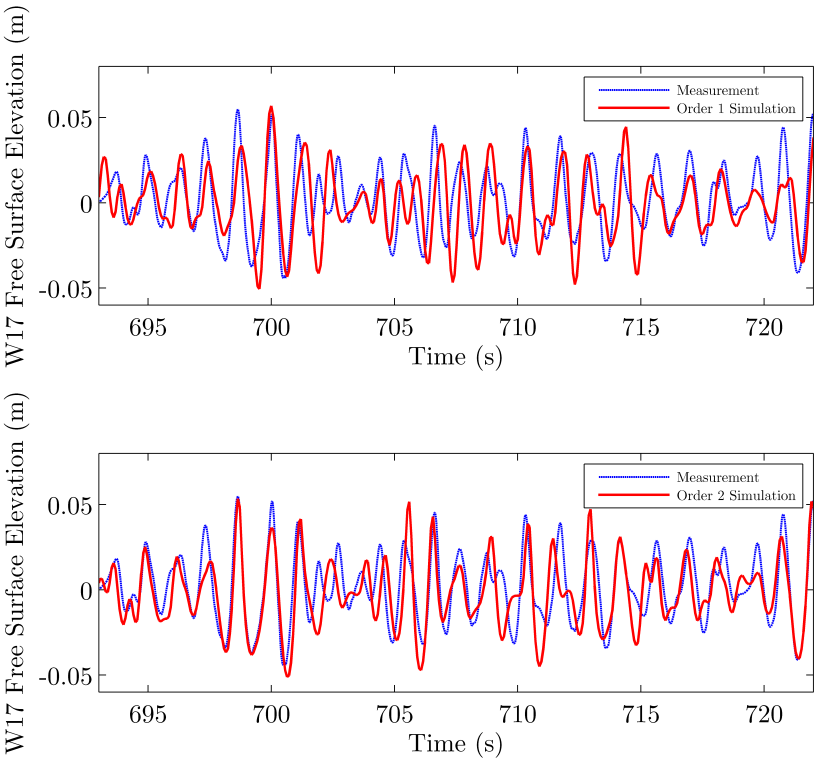

Figure IV.25: Comparison of measured and simulated wave signals at W17 from sloping bathymetry simulation

Benchmark simulation in 2HD: Monochromatic waves over a shoal

The experimental measurements of monochromatic waves over a shoal conducted by Berkhoff et al. [4] provide a challenging benchmark case for modeling and simulation of wave refraction and diffraction by complicated bathymetries. Monochromatic waves of period 1.0 s and amplitude $A_0 = 0.0232$ m are generated over a region of uniform depth 0.45 m to propagate towards an angled incline, upon which is positioned an ellipsoidal hump (Figure IV.26). Normalized maximum wave amplitudes observed during the

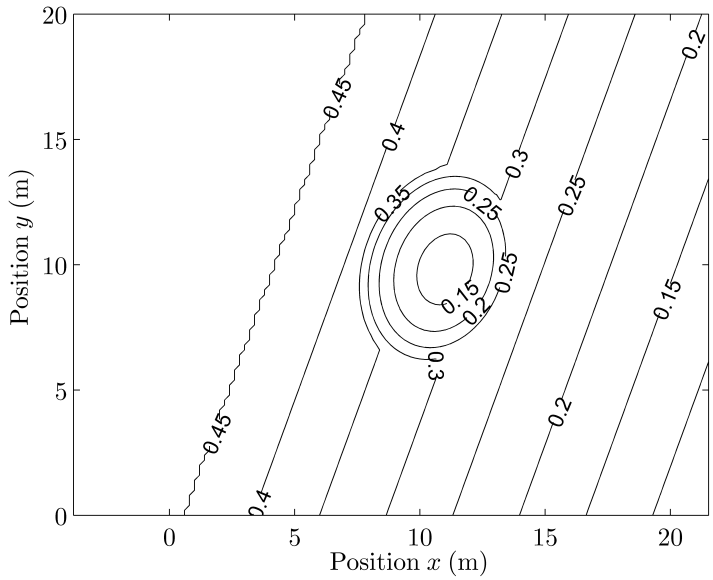

Figure IV.26: Depths (m) of the experimental bathymetry for 2HD shoal simulation

experiment were then recorded along cross-sectional segments.

The experiment is simulated here on the computational domain shown in Figure IV.27 with a 0.2-meter square grid. To reduce the influence of boundaries on wave heights near the shoal, and to provide an approximately uniform long-crested wave influx over the extent of the measurement area from a delta-function-type line source, the computational domain has extended slightly beyond the experimental domain, and undamped periodic conditions are retained in the upper and lower boundaries. At the left and right boundaries, waves encounter damping regions with characteristic function shown

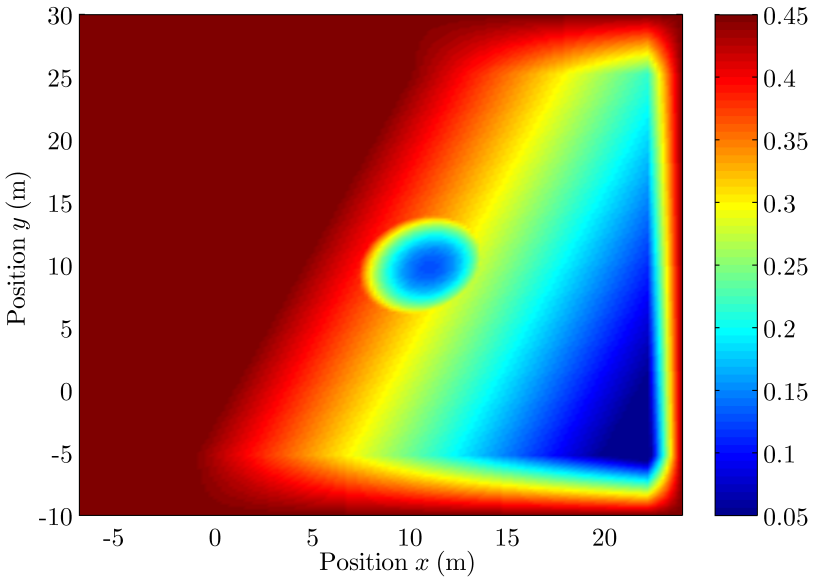

Figure IV.27: Depths (m) of the extended computational bathymetry for 2HD shoal simulation

in Figure IV.28.

For this bathymetry, a variable-depth composite operator is constructed using 3 representative depths operators with $h_1 = 0.05$ m, $h_2 = 0.2$ m, and $h_3 = 0.45$ m (Figure IV.29). Minimization of error with the weight function shown in Figure IV.30(a) yields coefficients (Figure IV.31) defining a combination operator with errors shown in Figure IV.30(b).

Images of free-surface elevations from the Order 1 Hamiltonian simulation demonstrate the expected refraction of waves propagating over the angled incline and diffraction over the shoal, apparently in reasonable accord with theoretical predictions made by Berkhoff et al. [4] (Figure IV.32). Normalized maximum wave heights observed over the course of the 45-s simulations are interpolated along 8 cross-sectional segments (Figure IV.33) and compared with the experimental measurements of Berkhoff et al. [4] for Order 1 (Figure IV.34) and Order 2 (Figure IV.35) simulations. While both models successfully capture many of the qualitative features of the data, the Order 2 simulation shows several noticeable improvements over the Order 1 simulation. Although both models overestimate the peak heights along sections 3 and 4, the Order 2 simulation predicts the measurements much more accurately, as is especially visible along cross sections 3, 4, 5, and 6.

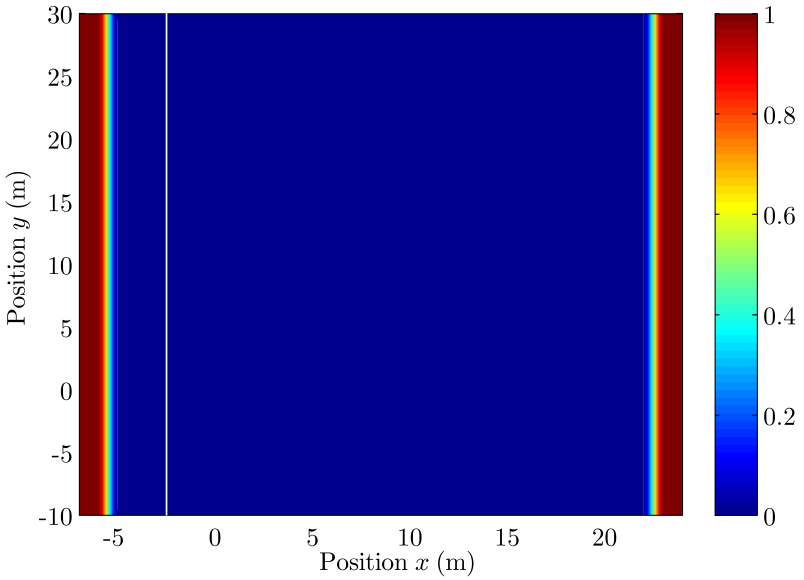

Figure IV.28: Magnitude of $\chi_D(x, y)$ for 2HD simulation and line source position (in white)

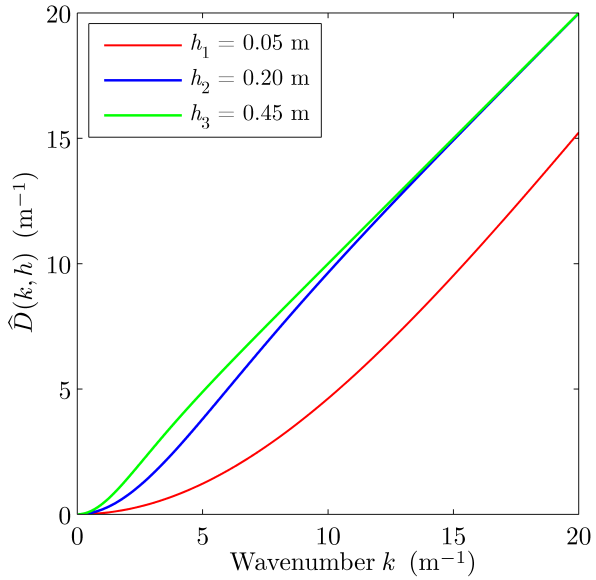

Figure IV.29: Representative-depth operators for 2HD shoal simulation

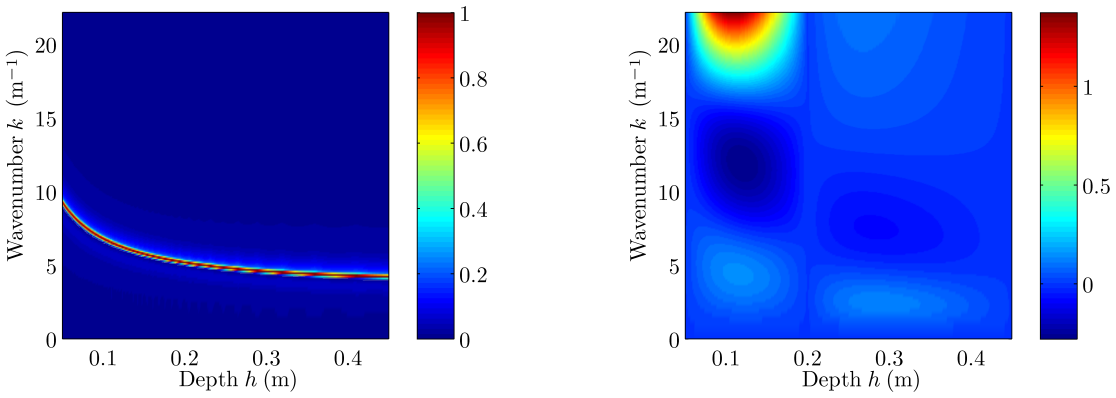

(a) $w(h,k)$ (b) $\hat{D}_{\approx}(h,k) - \hat{D}(h,k)$ (m^{-1})

Figure IV.30: (a) Weight function and (b) errors (m^{-1}) on $\hat{D}_{\approx}(h,k)$ for 2HD shoal simulation

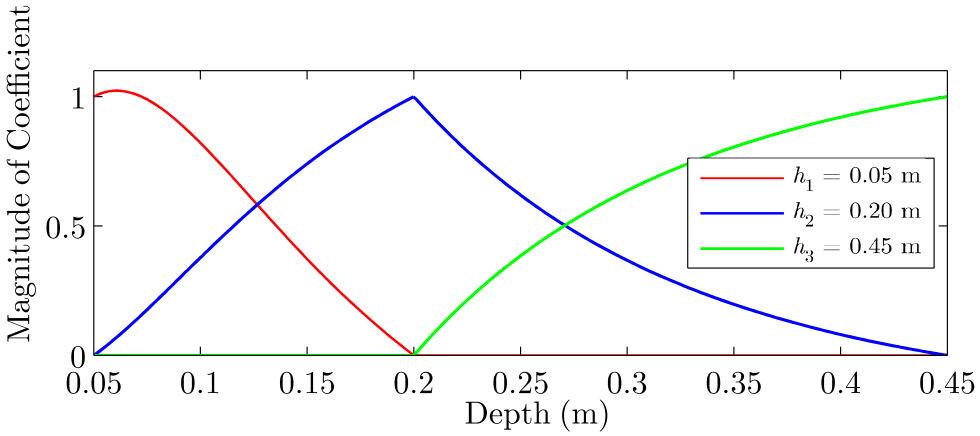

Figure IV.31: Representative-depth operators coefficients for 2HD shoal simulation

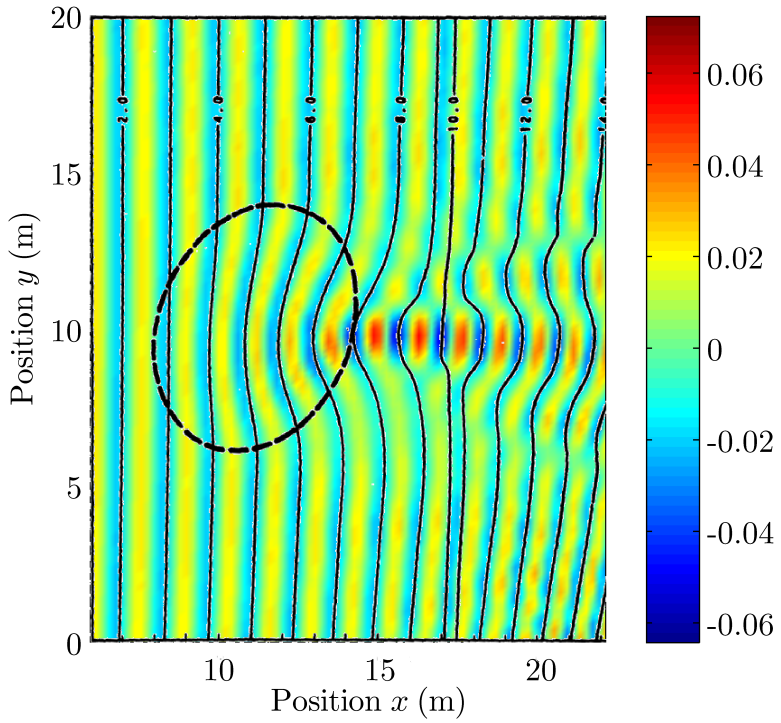

Figure IV.32: Free surface elevations (m) at $t = 45$ s with superimposed "lines of equal phase" by Berkhoff et al. [4] (solid lines) and shoal outline (dotted line)

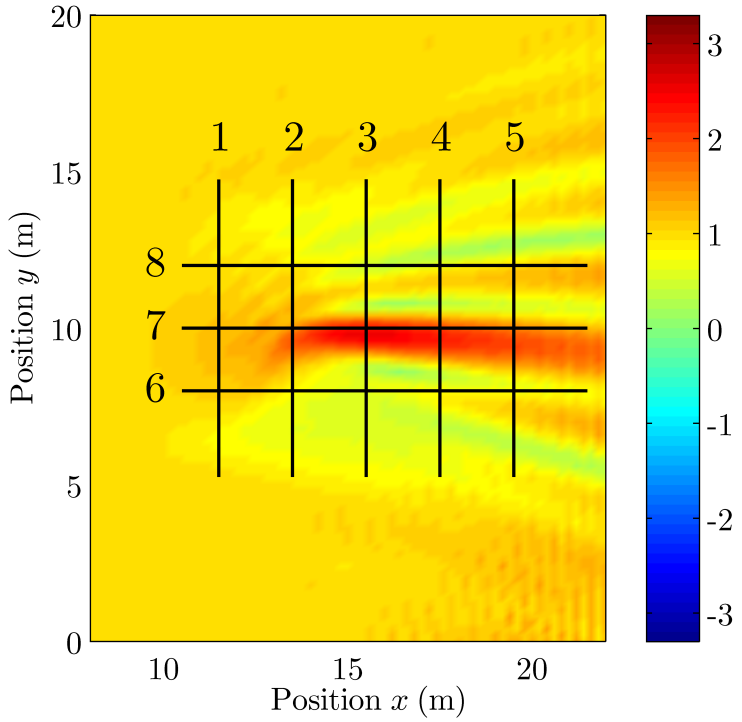

Figure IV.33: Maximum normalized wave heights $\frac{A}{A_0}$ from 2HD shoal simulation with superimposed cross sections

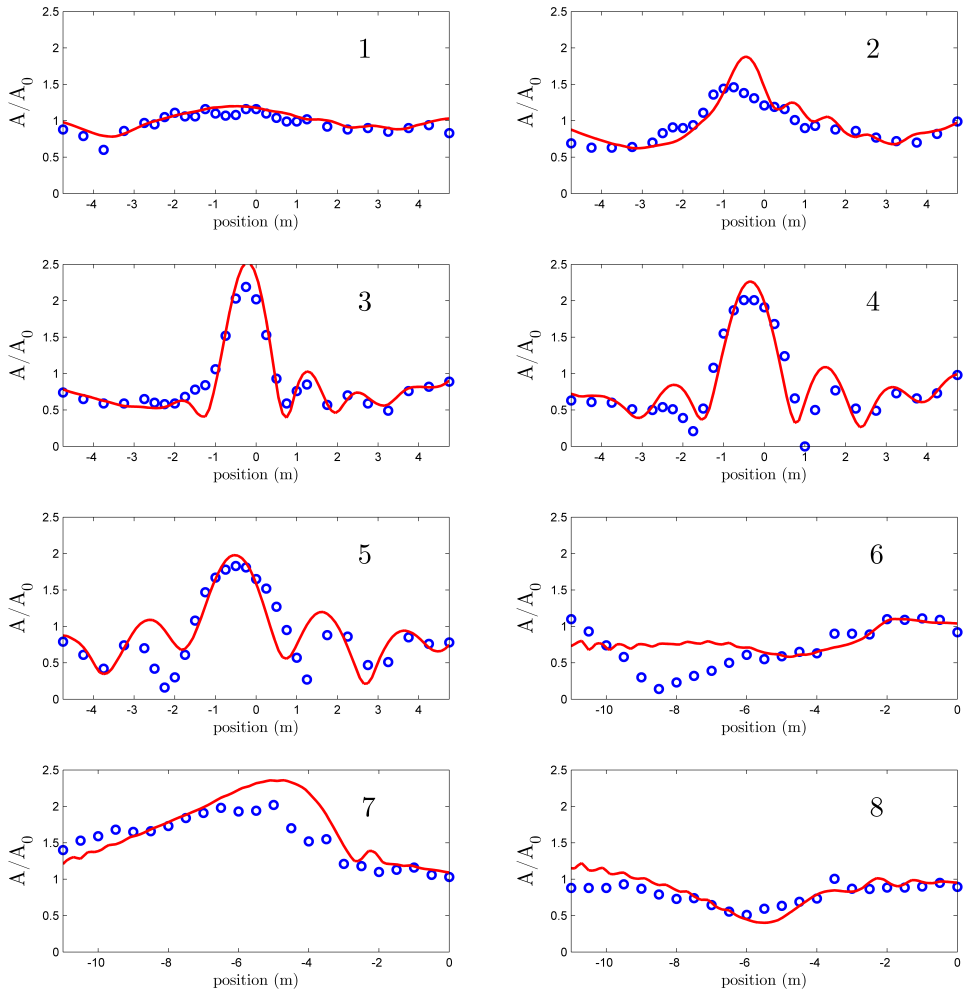

Figure IV.34: Comparison of maximum normalized wave heights (red) from Order 1 simulation with measurements (blue) from 2HD shoal experiment

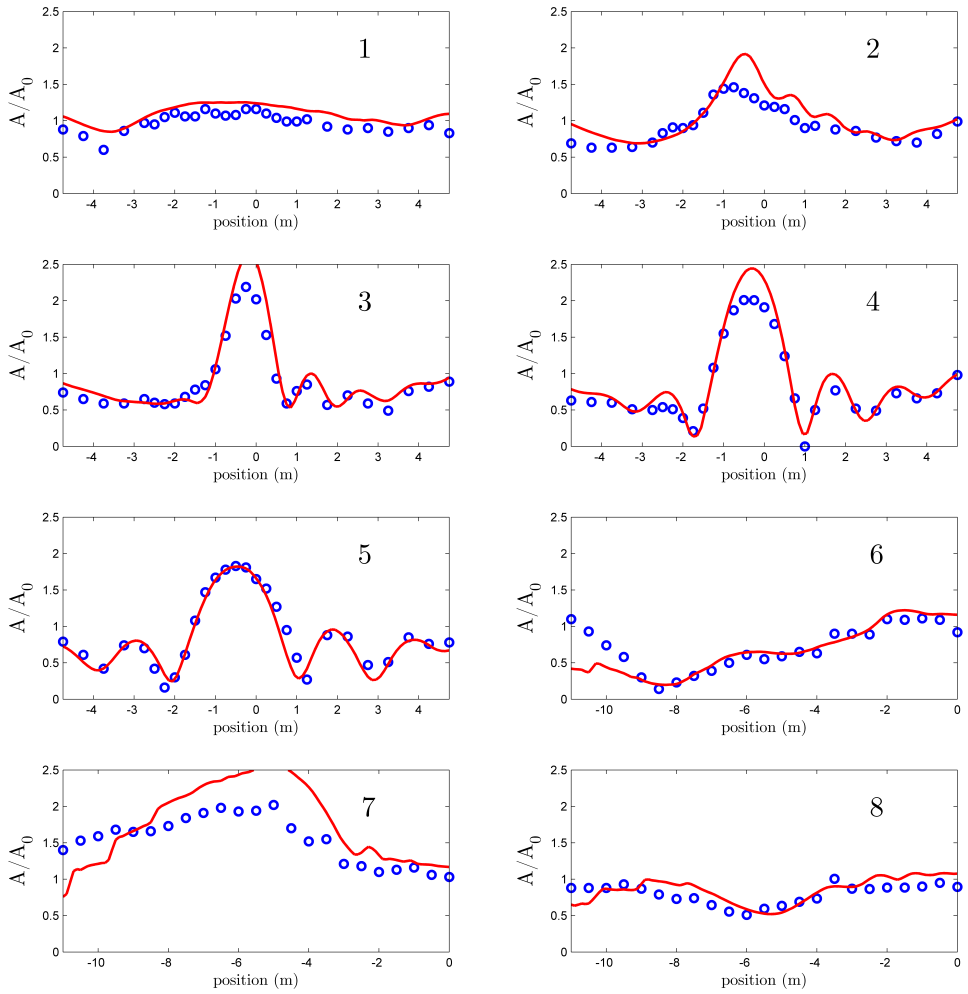

Figure IV.35: Comparison of maximum normalized wave heights (red) from Order 2 simulation with measurements (blue) from 2HD shoal experiment

Comparison with simulation results produced using a different model and numerical scheme demonstrate the pseudospectral Hamiltonian approach to be a competitive alternative. The results of the Order 1 pseudospectral Hamiltonian simulation are observed to resemble those from a nonlinear Variational Boussinesq Model simulation of Adytia [3] (Figure IV.36), implemented using a finite element method on a triangular grid with average grid spacing of about 0.10 m. The pseudospectral linear Hamiltonian simulation, performed here on a coarser square grid of 0.20-m spacing, was computed on a typical desktop computer on the order of the physical time. These results demonstrate

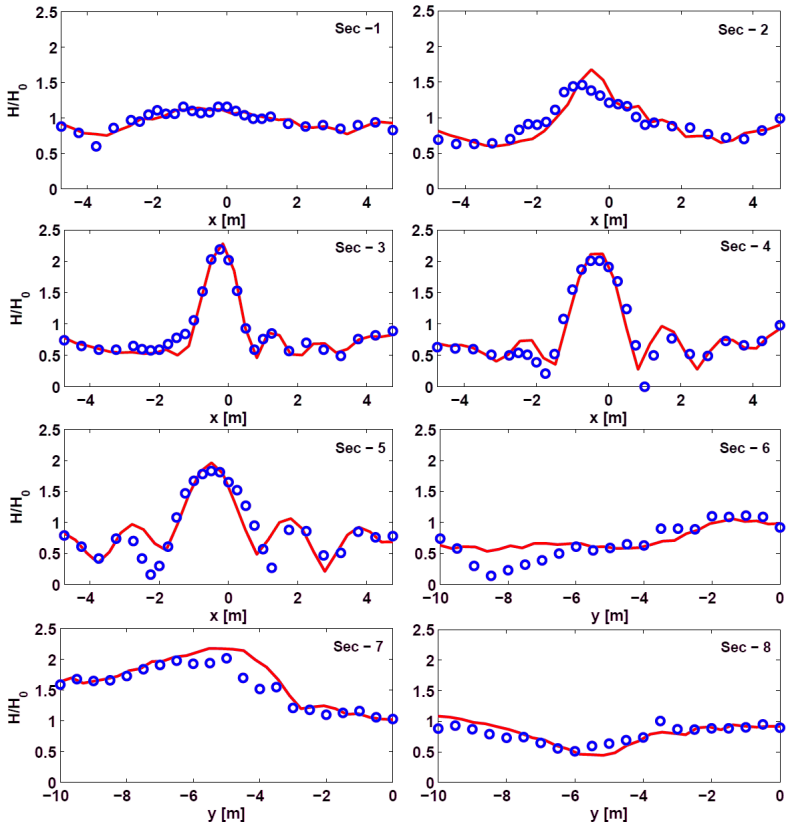

Figure IV.36: Comparison of maximum normalized wave heights (red) from Variational Boussinesq Model simulation with measurements (blue) from 2HD shoal experiment

the ability of the approach to model the effects of bathymetric variations in 2HD above complicated bathymetries such as those encountered in coastal waters, with higher-order models offering significantly improved accuracy.

CHAPTER V

SIMULATIONS OF WAVES OVER COASTAL BATHYMETRIES

Tsunami off southwest Java, Indonesia

To demonstrate the applicability to real coastal bathymetries of the methods discussed and validated in the previous chapters, simulations of two very different wave scenarios are conducted. First, propagation of a tsunami towards a coastline is simulated. Tsunami waves, generated by sudden seismic shifts in seafloor depth along faultlines which rapidly displace the surrounding water, are often simulated using initial value problems. Here, the pseudospectral Hamiltonian code is used to follow the example of Adytia [2], who used a Variational Boussinesq Model and Finite Element Method to simulate the tsunami which struck the southwest coast of Java, Indonesia on July 17, 2006.

For this simulation, the bathymetry in Figure V.1, obtained from the General Bathymetric Chart of the Oceans database (http://www.gebco.net/), is extended beyond the area shown and tapered off to a uniform depth at the computational domain boundaries to accomodate the use of damping regions around the simulated domain. This extended computational domain spans an area of 314 m by 330 km with a grid spacing of 2 km. A characteristic function $\chi_R(x, y)$, with values of 1 on land (pictured in white in Figure V.1) and 0 in water is used to roughly simulate wave reflections from coastlines. The variable-depth combination operator is constructed using representative depths $h_1 = 20$ m, $h_2 = 350$ m, $h_3 = 1500$ m, and $h_4 = 4000$ m. The weight function $w(h, k)$ used to compute coefficients for the representative-depth operators comes from

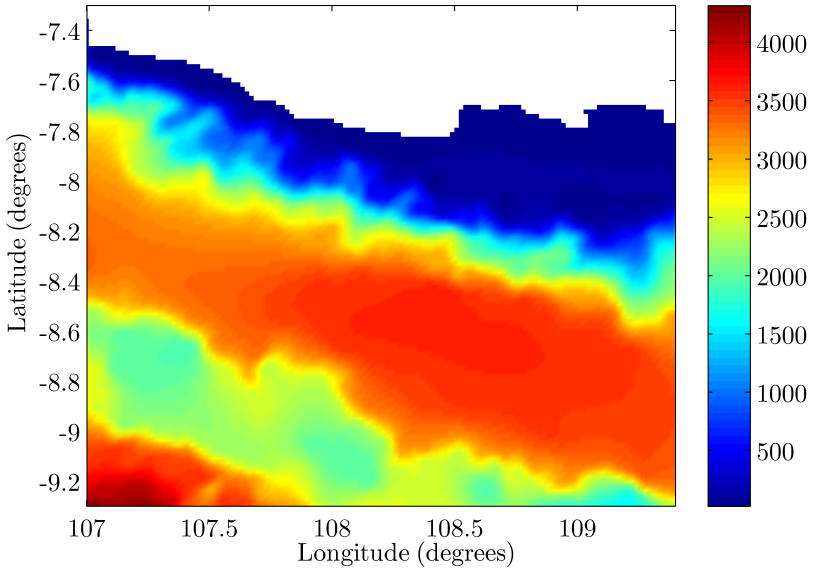

Figure V.1: Depths (m) of bathymetry for southwest Java tsunami simulation

the spatial Discrete Fourier Transform of the initial condition $\eta_0(x, y)$ considered as a function of frequencies ω associated with the wavenumbers k by the dispersion relation evaluated for $h(x_0, y_0) = 2424$ m, the local depth at the center (x_0, y_0) of the inital free surface disturbance feature. The envelope of a plot of these amplitudes versus frequencies is used to roughly characterize the shape of a "spectrum" which is then used in the same way as was the spectrum $s(t)$ in (II.75) to construct $w(h, k)$. This weight function $w(h, k)$ (Figure V.2(a)) produces a variable-depth operator with the errors shown in Figure V.2(b).

An initial condition resembling that used by Adytia [2] attempts to approximate the free surface disturbance caused by subduction of plates occuring at the fault, beginning from zero velocity at its maximum displacement (Figure V.3(a)). Progression of this initial condition towards the coast, as simulated with the Order 1 Hamiltonian model, is illustrated in Figure V.3(b)–(d). The maximum wave heights recorded over the course of the 25-minute simulation (Figure V.4) indeed resemble those from the simulations of Adytia [2] (Figure V.5), although the initial condition, treatment of wave reflection by coastlines, and simulation lengths differ.

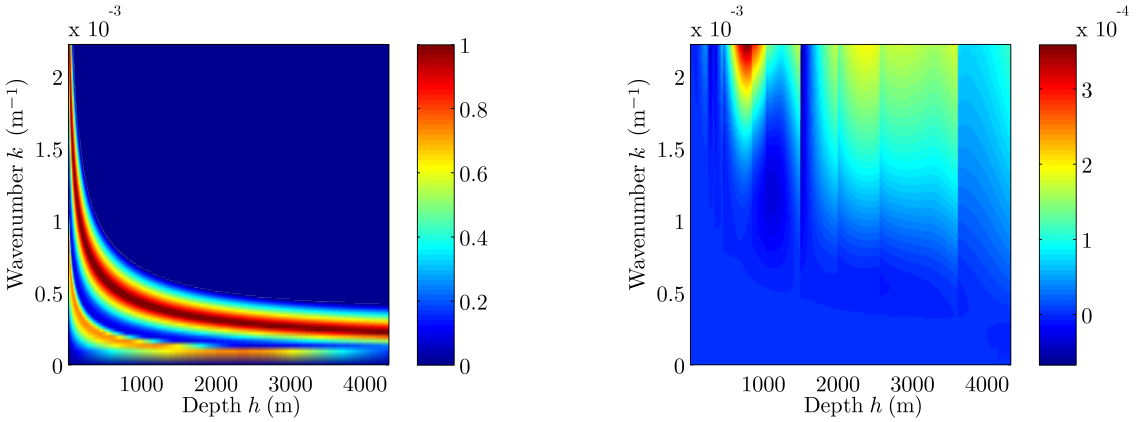

(a) $w(h,k)$ (b) $\hat{D}_{\approx}(h,k) - \hat{D}(h,k)$ (m^{-1})

Figure V.2: (a) Weight function and (b) errors (m^{-1}) on $\hat{D}_{\approx}(h,k)$ for southwest Java tsunami simulation

Wind waves at Pelabuhan Ratu, West Java, Indonesia

Pelabuhan Ratu is a fishing harbor located on the southern coast of West Java, Indonesia. Extreme waves in the harbor in recent years have caused damage to coastal structures and prompted evacuations and temporary suspensions of fishing activities. We simulate wind-generated waves in the region with bathymetry shown in Figure V.6, extended significantly beyond the boundaries shown to accomodate damping regions and a line source to influx waves under an angle so that waves reach the entirety of simulated domain. The extended computational domain spans an area of 1950 m by 2317.5 m with a grid spacing of 7.5 m. A reflective coastline is implemented as in the previous section.

Studies of the surrounding areas using SWAN (http://www.swan.tudelft.nl/), a software package for coastal wave simulations, suggest that typical waves entering the western boundary of the domain have a peak period of around 7 s and an amplitude of approximately 1.5 m, oriented at an angle of about 15^o North of East. In order to clearly illustrate the effects of the bathymetry on long-crested waves, monochromatic

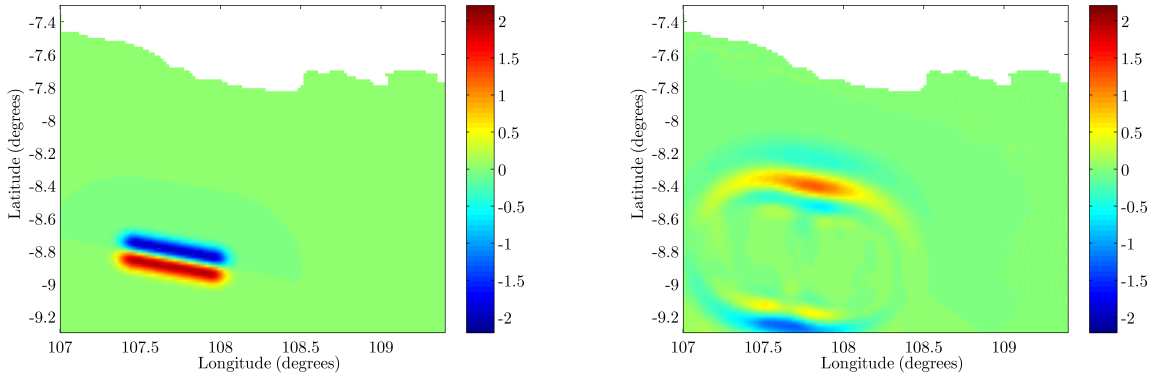

(a) $t = 0$ min

(b) $t = 6$ min

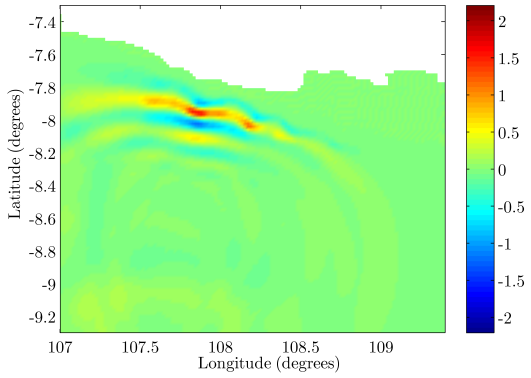

(c) $t = 12$ min

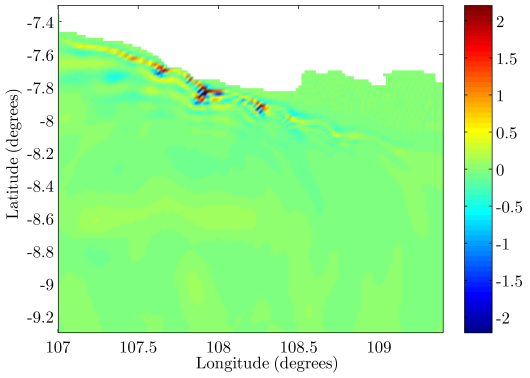

(d) $t = 18$ min

Figure V.3: Free surface heights (m) from Order 1 simulation of southwest Java tsunami simulation

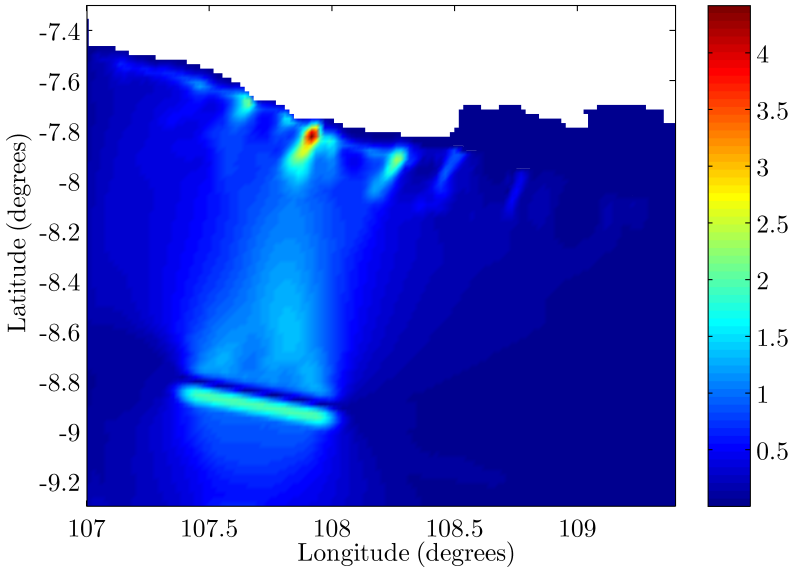

Figure V.4: Maximum free surface heights (m) from Order 1 simulation of southwest Java tsunami over $t = 0$ to 25 minutes

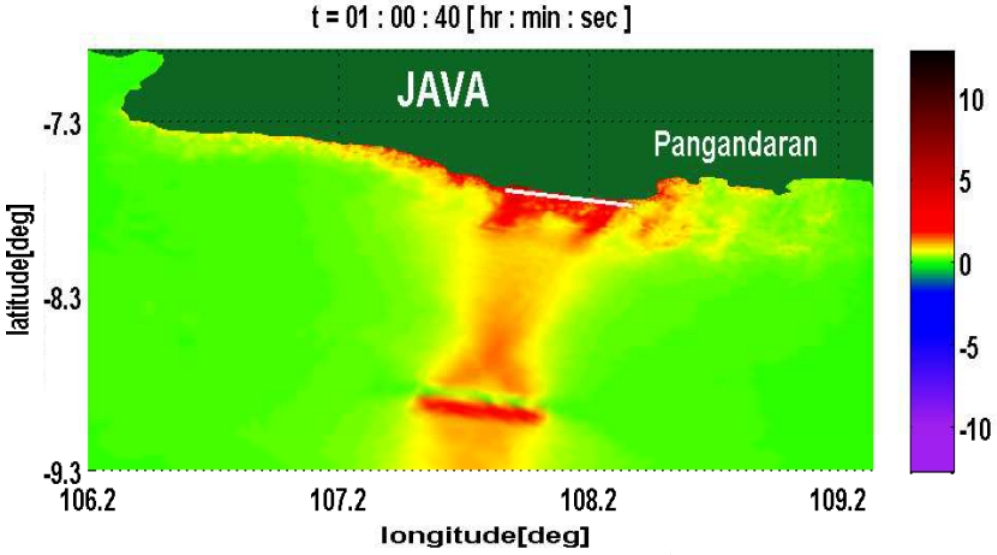

Figure V.5: Maximum free surface heights (m) from simulation of southwest Java tsunami from Adytia [2] over $t = 0$ to 60 minutes

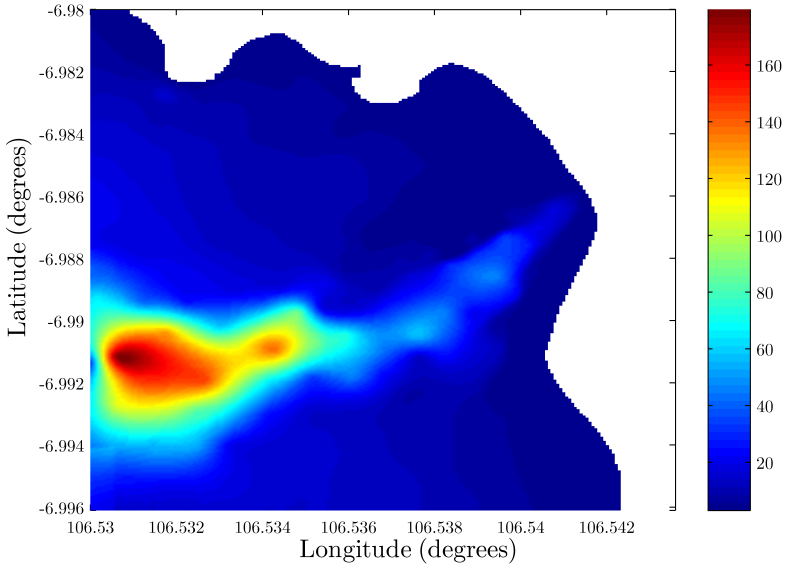

Figure V.6: Depths (m) of bathymetry for Pelabuhan Ratu simulation

waves with period 7 s are influxed here rather than a more realistic, broader wind wave spectrum. The variable-depth combination operator is constructed using representative depths $h_1 = 3$ m, $h_2 = 10$ m, $h_3 = 27.4$ m, and $h_4 = 179.6$ m and the weight function shown in Figure V.7(a), with resulting errors shown in Figure V.7(b).

Waves influxed from a vertical line-segment source located to the west of the simulation domain enter the initially undisturbed free surface and are refracted and diffracted by the bathymetry and reflected by the coastline as seen over the entire computational domain in Figure V.8. The wave field after the initial waves have reached the shore (Figure V.9), as well as the maximum wave heights recorded over the course of the 350 s simulation (Figure V.10), demonstrates that for uniform incoming waves, bathymetric effects lead to a large variety of wave heights at within the harbor and along the coastline.

Computations of significant wave heights based on SWAN simulations for the same bathymetry (Figure V.11) appear to show a qualitative correspondence with the Order 1 Hamiltonian predictions of maximum wave height. Areas showing the highest significant wave height in the SWAN prediction very nearly coincide with those areas at which the highest waves were predicted by the Hamiltonian simulation, with common regions of relative calm also predicted by both approaches.

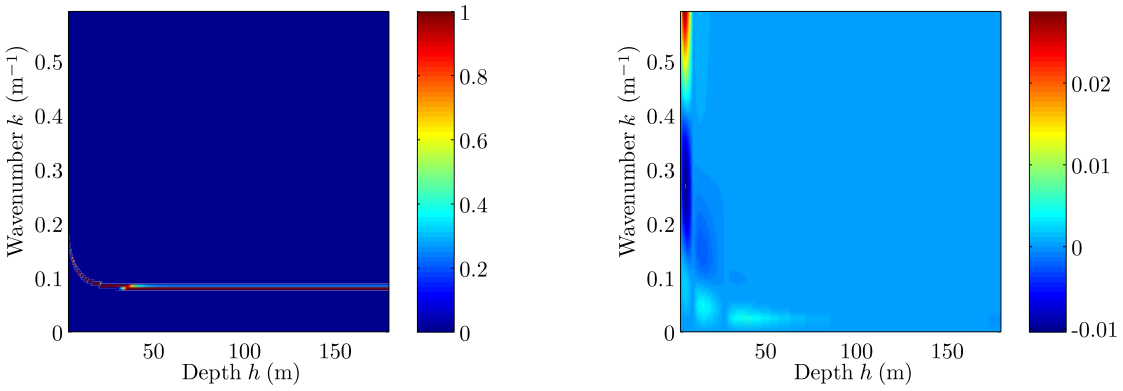

(a) $w(h,k)$ (b) $\hat{D}_{\approx}(h,k) - \hat{D}(h,k)$ (m^{-1})

Figure V.7: (a) Weight function and (b) errors (m^{-1}) on $\hat{D}_{\approx}(h,k)$ for Pelabuhan Ratu simulation

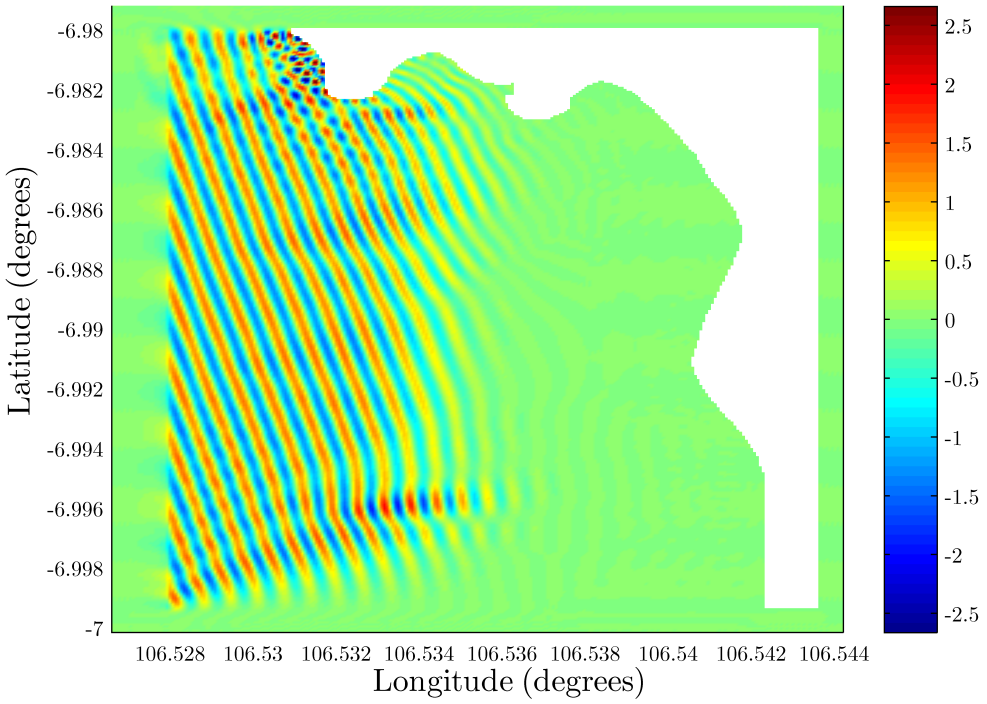

Figure V.8: Free surface elevations (m) at $t = 170$ s from Order 1 simulation of Pelabuhan Ratu wind waves

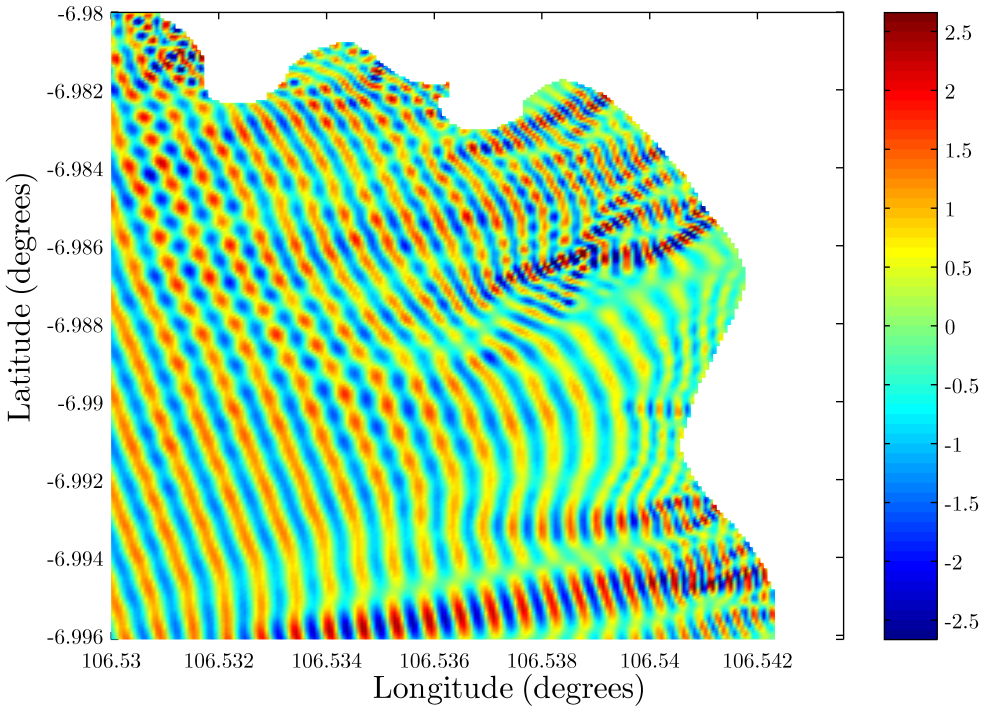

Figure V.9: Free surface elevations (m) at $t = 340$ s from Order 1 simulation of Pelabuhan Ratu wind waves

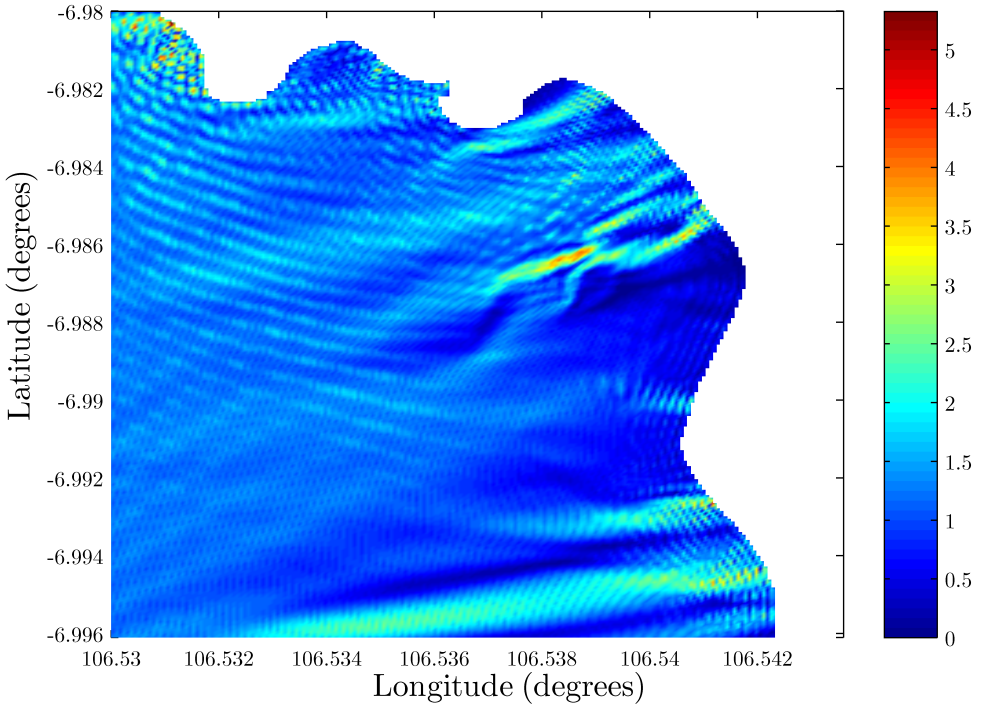

Figure V.10: Maximum free surface elevations from $t = 0$ to 350 s from Order 1 Hamiltonian simulation

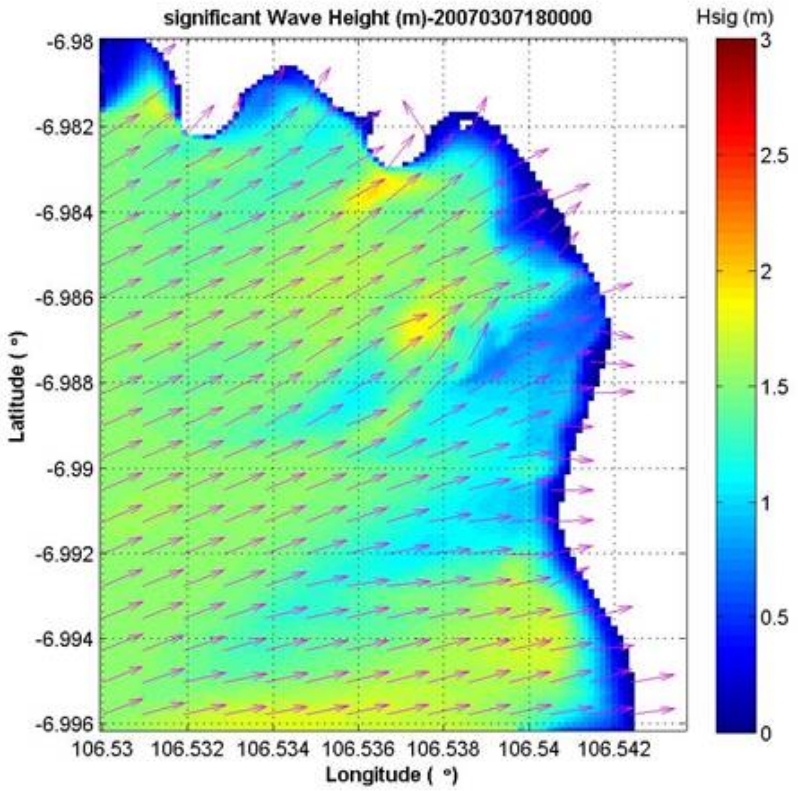

Figure V.11: Significant wave heights (m) computed in SWAN simulation over Pelabuhan Ratu bathymetry

CHAPTER VI

CONCLUSIONS

The pseudospectral implementation of Hamiltonian dynamical equations described in this thesis performed well in a variety of challenging benchmark simulations. First, its ability to conserve the approximated total energy expressed by the Hamiltonian function for simulations over uniform-depth regions was confirmed. Over varying-depth bathymetries, this property appears to still hold approximately true, but slight shifts in the value of the Hamiltonian were observed for wave features propagating over bathymetric variations under the nonlinear Hamiltonian equations. Further study of this phenomenon may be necessary to understand its implications for the accuracy and stability of the method.

The accurate modeling of linear wavelength dispersion by the model was demonstrated through simulation of a focusing wave group experiment. Its modeling of bathymetric effects by extension of the pseudodifferential operator from the constant-depth equations to a variable-depth combination operator was validated through simulation of irregular waves propagating over a slope. The method's ability to simulate refraction and diffraction of waves over elaborate 2HD bathymetries was also validated in simulation of the experiment of Berkhoff et al. [4], with performance resembling that of more computationally expensive schemes. While the method's accurate handling of bathymetric effects was validated, some details of the approach used could be studied more deeply. Generalizing the method of "quasi-homogenization" of constant-depth pseudodifferential operators used by van Groesen and van der Kroon [13], we introduced a flexible method for constructing the combination operator so as to minimize its error from the true constant-depth operator in a way which is fine-tuned to the needs of individual simulations. However, the improvements in accuracy which this approach may offer have

not been rigorously quantified, nor have we clarified to what extent the use of additional representative depths in the construction of this operator may improve results.

In all of the test cases investigated here, the Order 2 model almost always succeeded to offer visible improvements in accuracy over the Order 1 model, especially for relatively large-amplitude wave features, demonstrating the potential of higher-order versions of the dynamical equations to accurately capture important nonlinear effects. This improvement does not necessarily carry through to arbitrarily high order, however, as computational times increase steeply for higher-order models, and the measures required to prevent aliasing due for nonlinearities of higher order increasingly filter out important information in some cases. For the particular benchmark case and computational resolution for which the Order 3 and Order 4 models were tested here, results were actually less accurate than for the Order 2 simulation. Still, in its Order 1 and Order 2 versions, the pseudospectral Hamiltonian approach has been shown to be consistently competitive, and in some cases superior to, other schemes.

Simulations of tsunami and wind-type wave groups over actual coastal bathymetries demonstrated the feasibility of the pseudospectral Hamiltonian approach to simulate a variety of realistic coastal wave scenarios at different scales. While the method used can indeed provide useful information about wave run-up towards coastlines, wave dynamics in near-shore environments are significantly influenced by several factors which are not yet addressed in the implementation presented here. Consideration of factors such as wave breaking and bottom friction could make for more realistic simulations, although incorporation of these features may not be trivially straightforward in the context of the pseudospectral method used here. Also, although in the simulations presented here roughly simulated wave reflections from coastlines using reflective damping terms, a more physically-realistic method of modeling of this reflection could perhaps be achieved through the use of source terms to influx wave reflections into the domain at reflective interfaces. Similarly, a use of source terms to simulating waves generated by moving objects embedded in the domain could be useful for many applications.

While prediction of the heights of waves approaching coastlines is certainly useful, the

details of coastal inundation by incoming waves is of interest in some applications. Once again, incorporation of this effect into the pseudospectral Hamiltonian scheme may be challenging. And, while free surface heights themselves are often the primary quantity of interest, many applications involving wave-structure interactions also benefit from information about quantities in the fluid interior. Incorporation of methods for recovering estimates of interior pressures from the surface variables could be a useful addition to the code.

These and many other issues have yet to be addressed, and may require attention before this pseudospectral implementation of Hamiltonian surface water wave equations could be presented as a stable, versatile tool to compete with more ubiquitous schemes and software packages that are typically used in coastal wave research and industry. However, based on the promising results of the simulations presented in this thesis, it seems clear that further research along these lines could indeed be worthwhile.

Bibliography

[1] M.J. Ablowitz and T.S. Haut. Spectral formulation of the two fluid Euler equations with a free interface and long wave reductions. *Analysis and Applications*, 6(04): 323–348, 2008.

[2] Didit Adytia. Tsunami simulation in Indonesia's areas based on shallow water equations and Variational Boussinesq Model using finite element method. Master's thesis, Institut Teknologi Bandung, 2008.

[3] Didit Adytia. *Coastal zone simulations with Variational Boussinesq Modelling*. PhD thesis, University of Twente, 2012.

[4] J.C.W. Berkhoff, N. Booy, and A.C. Radder. Verification of numerical wave propagation models for simple harmonic linear water waves. *Coastal Engineering*, 6:255–279, 1982.

[5] L.J.F. Broer. On the Hamiltonian theory of surface waves. *Applied Scientific Research*, (30):430–446, 1974 1974.

[6] T.H.J. Bunnik. Benchmark workshop on numerical wave modelling - description of test cases. Technical Report 70022-1-RD, Maritime Research Institute Netherlands, August 2010.

[7] W. Craig and C. Sulem. Numerical simulation of gravity waves. *Journal of Computational Physics*, 108:73–83, 1993.

[8] Stanislav Derevyanko. The $(n+1)/2$ rule for dealiasing in the split-step Fourier methods for n-wave interactions. *Photonics Technology Letters, IEEE*, 20(23).

[9] Bengt Fornberg. *A practical guide to pseudospectral methods*. Cambridge university press, 1998.

[10] Gunwoo Kim, Changhoon Lee, and Kyung-Duck Suh. Internal generation of waves: Delta function method and source term addition method. *Ocean Engineering*, 34: 2251–2264, 2007.

[11] Lie She Liam. *Mathematical modelling of generation and forward propagation of dispersive waves*. PhD thesis, University of Twente, 2013.

[12] J.C. Luke. A variational principle for a fluid with a free surface. *Journal of Fluid Mechanics*, 27, part 2:395–397, 1967.

[13] E. van Groesen and I. van der Kroon. Fully dispersive dynamic models for surface water waves above varying bottom, part 2: Hybrid spatial-spectral implementations. *Wave Motion*, 49:198–211, 2012.

[14] Ge Wei, James T. Kirby, and Amar Sinha. Generation of waves in Boussinesq models using a source function method. *Coastal Engineering*, 36:271–299, 1999.

[15] V.E. Zakharov. Stability of periodic waves of finite amplitude on the surface of a deep fluid. *Journal of Applied Mechanics and Technical Physics*, 9, issue 2:190–194, March–April 1968.